Q. J. R. Meteorol. Soc. (1997), **123**, pp. 101–127

A new subgrid-scale orographic drag parametrization: Its formulation and testing

By FRANÇOIS LOTT and MARTIN J. MILLER*
European Centre for Medium-Range Weather Forecasts, UK

(Received 2 August 1995; revised 28 March 1996)

SUMMARY

A scheme for the representation of subgrid-scale orography (SSO) in numerical weather prediction and climate models is presented. The new scheme arose in part from a desire to represent nonlinear low-level mountain drag effects not currently parametrized. An important feature of the scheme is that it deals explicitly with a low-level flow which is 'blocked', when the effective height of the subgrid-scale orography is sufficiently high. In this new scheme, it is assumed that, for this 'blocked' flow, separation occurs at the mountain flanks, resulting in a form drag. This drag is parametrized on model levels which are intersected by the SSO, and provides a dynamically based replacement for envelope orography. The upper part of the low-level flow goes over the orography and generates gravity waves. At the model resolutions considered (T106 and T213) it is assumed that the length scales characteristic of the SSO are sufficiently small for the Coriolis force to be neglected. The various parameters of the scheme are adjusted using an off-line procedure in which the scheme is used to estimate the mountain drag and the momentum profiles above the Pyrenees; and these estimates are validated with the PYREX data. Forecasts using T106 and T213 resolutions with this new scheme, and with mean orography, show that the forecast mountain drag consistently reproduces the drag measured during PYREX whenever the flow component normal to the ridge is large. Isentropic flow diagnostics, further, show that the new scheme has a realistic impact on the flow dynamics, reinforcing the low-level wake observed in mesoscale analyses of the flow. With this new scheme and a *mean* orography, the ECMWF model outperformed, in forecast skill, a version of the model which had an envelope orography and the old gravity-wave-drag scheme, while no longer suffering any disadvantages of envelope orography. The proposed low-level drag parametrization should also be relevant at model horizontal resolutions much higher than T213.

KEYWORDS: Blocked flow Gravity waves Orographic drag Parametrization

1. INTRODUCTION

In many of the studies concerning the representation of orography in numerical weather prediction (NWP) and general circulation models (GCM), attention has been focused either on the parametrization of subgrid-scale mountain waves or on the optimal representation of the resolved mountain ranges. The first approach has led to the introduction of the gravity-wave-drag schemes (Boer *et al.* 1984; Palmer *et al.* 1986; Miller *et al.* 1989), and the second, for example, to the use of an envelope orography which improves the model representation of the large-scale planetary waves (Wallace *et al.* 1983). These studies dealt essentially with the impact of the subgrid-scale orography and of the resolved-scale orography on the global dynamics of the atmosphere. Recent studies of the local behaviour of the ECMWF model near the Pyrenees (Lott 1995) have shown that the model underestimates the mountain drag, and generates mountain waves which have a horizontal scale close to the model truncation and which are often not observed. Furthermore, the way these waves are dissipated and affect the flow is unclear and unrealistic. Clark and Miller (1991) have shown, using a nested high-resolution model, that there is a large underestimation of the total drag at horizontal resolutions coarser than about 10 km, which cannot adequately be made up by the use of an envelope orography. These results indicate that increasing the drag by using an envelope orography (Tibaldi 1986) is not a satisfactory technique for representing mountains in models. Furthermore, the envelope orography is detrimental to the data assimilation process since it results in more low-level data being

* Corresponding author: European Centre for Medium-Range Weather Forescasts, Shinfield Park, Reading, Berkshire, RG2 9AX, UK.

rejected when it is used. Envelope orography also tends to give excessive precipitation, especially from convection generated by the elevated heating of the enhanced orography. It may therefore be desirable to replace the envelope orography by a mean orography without further changes, but such a reduction of the mountain height will reduce the model mountain pressure drag with detrimental effect on the forecasts and model climate. The facts that the present gravity-wave-drag scheme represents low-level drag inadequately, and that the total mountain drag is already too low in the current model with envelope orography, indicate that a major revision of the representation of subgrid-scale orography (SSO) is desirable and necessary to successfully represent the overall impact of orography on global dynamics.

In the present work, it is assumed that, so far as the large scale is concerned, the model mean orography is the optimal representation. Although some justification has already been given for this particular choice, further justification can be provided from dynamical theory. The greatest force exerted by mountains on the atmosphere is lift, which is essentially perpendicular to the flow and varies with the mountains' volume (Smith 1979). This lift force accompanies the anticyclonic circulation that occurs above large-scale massifs in mid latitudes, and its dependence on the mountains' volume remains valid even if this lift force is reduced by the presence of a cold front (Egger and Hoinka 1992). Consequently, only forces due to the intersection of subgrid-scale mountains with model levels and those which arise from the generation of vertically propagating gravity waves need to be parametrized. In this context, a number of recent studies (e.g. Hunt and Snyder 1980; Smolarkiewicz and Rotunno 1989; Schär and Smith 1993) on nonlinear flow past three-dimensional orography have helped provide motivation in this study. Recent work by Baines and Palmer (1990) and Baines (1995) has presented the principles of a subgrid-scale orographic drag scheme in which particular emphasis is placed on the representation of the surface stress from three-dimensional waves. These authors also suggested that further drag should be provided at the model levels that intersect the subgrid-scale orography. In the following sections a theoretical formulation is proposed for a drag of this nature on model levels, and this forms a major component of the new subgrid-scale orographic drag scheme. In section 2 the general principles of the new scheme are presented interpreting results form theoretical studies of flow near mesoscale orography in the context of numerical weather prediction models. In section 3 the parametrization scheme is described in detail. In section 4, using an off-line procedure, the new scheme is used to predict the drag and the momentum flux profiles observed during the PYREX experiment. Section 5 of the paper contains an on-line validation of the scheme. The scheme is tested with the ECMWF model (at T106 and T213 resolutions), using forecast experiments covering the periods of intense observation of the PYREX campaign. At both resolutions, it appears that the model with the new scheme is able consistently to reproduce the measured pressure drag. Isentropic diagnostics of the flow dynamics are used to study the impact of the scheme on the dynamics of the low-level flow. In section 6 there is a summary of some experimental forecast results comparing performances of the model using mean orography, with and without the new scheme, and with a version of the model using envelope orography and the old gravity-wave-drag scheme that has been used operationally at ECMWF.

2. General principles of the new scheme

The new scheme is based on ideas presented by Baines and Palmer (1990) combined with ideas from bluff-body dynamics. The assumption is that the mesoscale flow dynamics can be described by two conceptual models, whose relevance depends on the

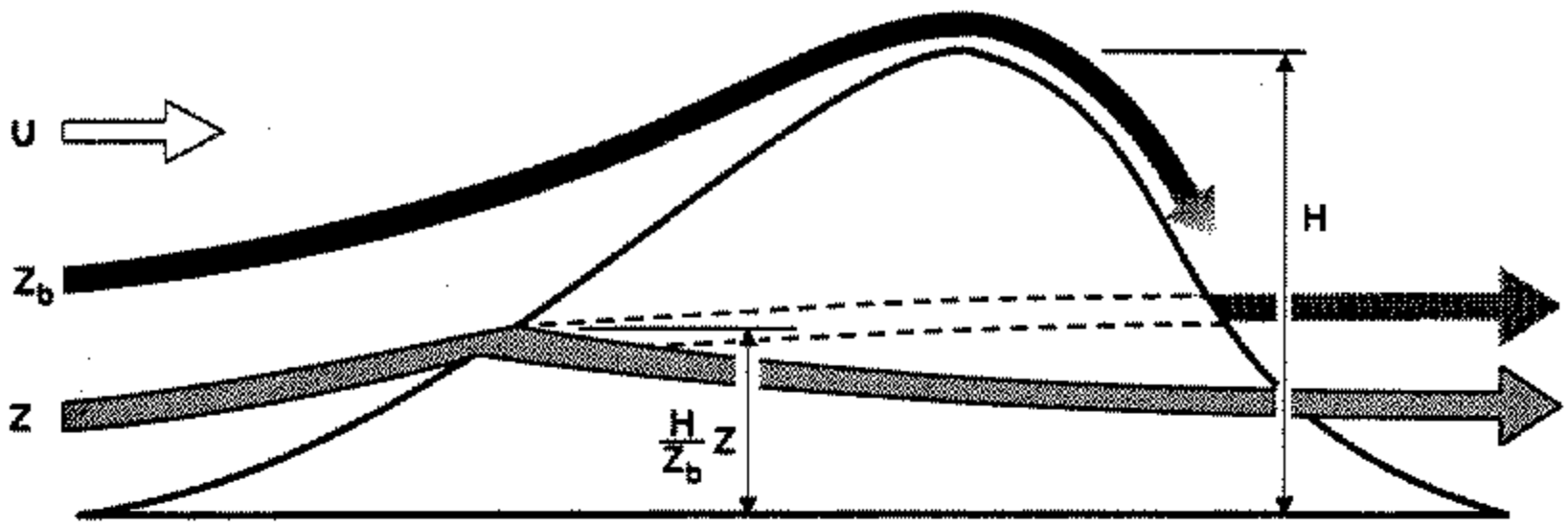

Figure 1. Schematic representation of the low-level flow behaviour parametrized in the new scheme (see text for details.

non-dimensional height of the mountain, viz.

$$H_n \equiv \frac{NH}{|U|} \tag{1}$$

where H is the maximum height of the obstacle, U is the wind speed and N is the Brunt–Väisälä frequency of the incident flow.

At small H_n, all the flow goes over the mountain and gravity waves are forced by the vertical motion of the fluid. Suppose that the mountain has an elliptical shape and a height variation determined by a parameter b in the along-ridge direction and by a parameter a in the cross-ridge direction, such that

$$\gamma = a/b \leqslant 1,$$

then the geometry of the mountain can be written in the form

$$h(x, y) = \frac{H}{1 + x^2/a^2 + y^2/b^2}. \tag{2}$$

In the simple case when the incident flow is at right angles to the ridge the surface stress due to the gravity wave has the magnitude

$$\tau_w = \rho_0 \, bGB(\gamma)NUH^2 \tag{3}$$

provided that the Boussinesq and hydrostatic approximations apply. In Eq. (3) G is a function of the mountain sharpness (Phillips 1984), and for the mountain given by Eq. (2), $G \approx 1.23$. The term $B(\gamma)$ is a function of the mountain anisotropy, γ, and can vary from $B(0) = 1$ for a two-dimensional ridge to $B(1) = \pi/4$ for a circular mountain.

At large H_n, the vertical motion of the fluid is limited and part of the low-level flow goes around the mountain. As is explained in section 3, the depth, Z_b, of this blocked layer, when U and N are independent of height, can be expressed as

$$Z_b = H \max\left(0, \frac{H_n - H_{nc}}{H_n}\right) \tag{4}$$

where H_{nc} is a critical non-dimensional mountain height of order unity. The depth Z_b can be viewed as the upstream elevation of the isentropic surface that is raised exactly to the mountain top (Fig. 1). In each layer below Z_b the flow streamlines divide around the obstacle, and it is supposed that flow separation occurs on the obstacle's flanks. Then, the drag, $D_b(z)$, exerted by the obstacle on the flow at these levels can be written as

$$D_b(z) = -\rho_0 \, C_d \, l(z) \frac{U|U|}{2}. \tag{5}$$

Here $l(z)$ represents the horizontal width of the obstacle as seen by the flow at an upstream height z, and C_d, according to the free streamline theory of jets in ideal fluids, is a constant having a value close to unity (Kirchoff 1876; Gurevich 1965). According to observations, C_d can be nearer 2 in value when suction effects occur in the rear of the obstacle (Batchelor 1967). In the proposed parametrization scheme this drag is applied to the flow, level by level, and will be referred to as the drag of the 'blocked' flow, D_b. Unlike the gravity-wave-drag scheme, the total stress exerted by the mountain on the 'blocked' flow does not need to be known *a priori*. For an elliptical mountain, the width of the obstacle, as seen by the flow at a given altitude $z < Z_b$, is given by

$$l(z) = 2b\left(\frac{Z_b - z}{z}\right)^{1/2}. \tag{6}$$

In Eq. (6), it is assumed that the level Z_b is raised up to the mountain top, with each layer below Z_b raised by a factor H/Z_b (Fig. 1). This will lead, effectively, to a reduction of the obstacle width, as seen by the flow when compared with the case in which the flow does not experience vertical motion as it approaches the mountain. Then applying Eq. (5) to the fluid layers below Z_b, the stress due to the blocked-flow drag is obtained by integrating from $z = 0$ to $z = Z_b$, viz.

$$\tau_b \approx C_d \pi b \rho_0 Z_b \frac{U|U|}{2}. \tag{7}$$

However, when the non-dimensional height is close to unity, the presence of a wake is generally associated with upstream blocking and with a downstream foehn (e.g. Fig. 1). This means that the isentropic surfaces are raised on the windward side and become close to the ground on the leeward side. If we assume that the lowest isentropic surface passing over the mountain can be viewed as a lower rigid boundary for the flow passing *over* the mountain, then the distortion of this surface will be seen as a source of gravity waves, and since this distortion is of the same order of magnitude as the mountain height, it is reasonable to suppose that the wave stress will be given by Eq. (3), whatever the depth of the blocked flow, Z_b, although it is clearly an upper limit to use the total height, H. Then, the total stress is the sum of a wave stress, τ_w, and a blocked-flow stress whenever the non-dimensional mountain height $H_n > H_{nc}$, i.e.

$$\tau \approx \tau_w \left\{1 + \frac{\pi C_d}{2GB(\gamma)} \max\left(0, \frac{H_n - H_{nc}}{H_n^2}\right)\right\}. \tag{8}$$

The addition of low-level drag below the depth of the blocked flow, Z_b, enhances the gravity-wave stress term in Eq. (8) substantially. Figure 2 shows the ratio between the total stress and the wave stress as a function of H_n for two pairs of the parameters C_d, H_{nc}, and gives a comparison with the pressure drag measured during two numerical experiments with uniform stratified flow incident over, in one case, a two-dimensional ridge (Stein 1992) and, in the other, a three-dimensional ridge (Miranda and James 1993). In these comparisons, it is assumed that the nonlinear enhancement of the drag observed in the two-dimensional simulations corresponds to the drag enhancement that should occur in a flow normal to a very elongated ridge. When comparing the measurements obtained from Eq. (8) with the results of Miranda and James (1993) the differences in the mountain shapes as used by these authors, and as given by Eq. (2), were neglected. Figure 2 shows that the estimation of two-dimensional drags by this conceptual model is good for $C_d = 2$, $H_{nc} = 0.4$. Since there is substantial upstream blocking in these two-dimensional simulations when the non-dimensional height H_n exceeds 2 (Stein 1992), the large value of C_d simulates this

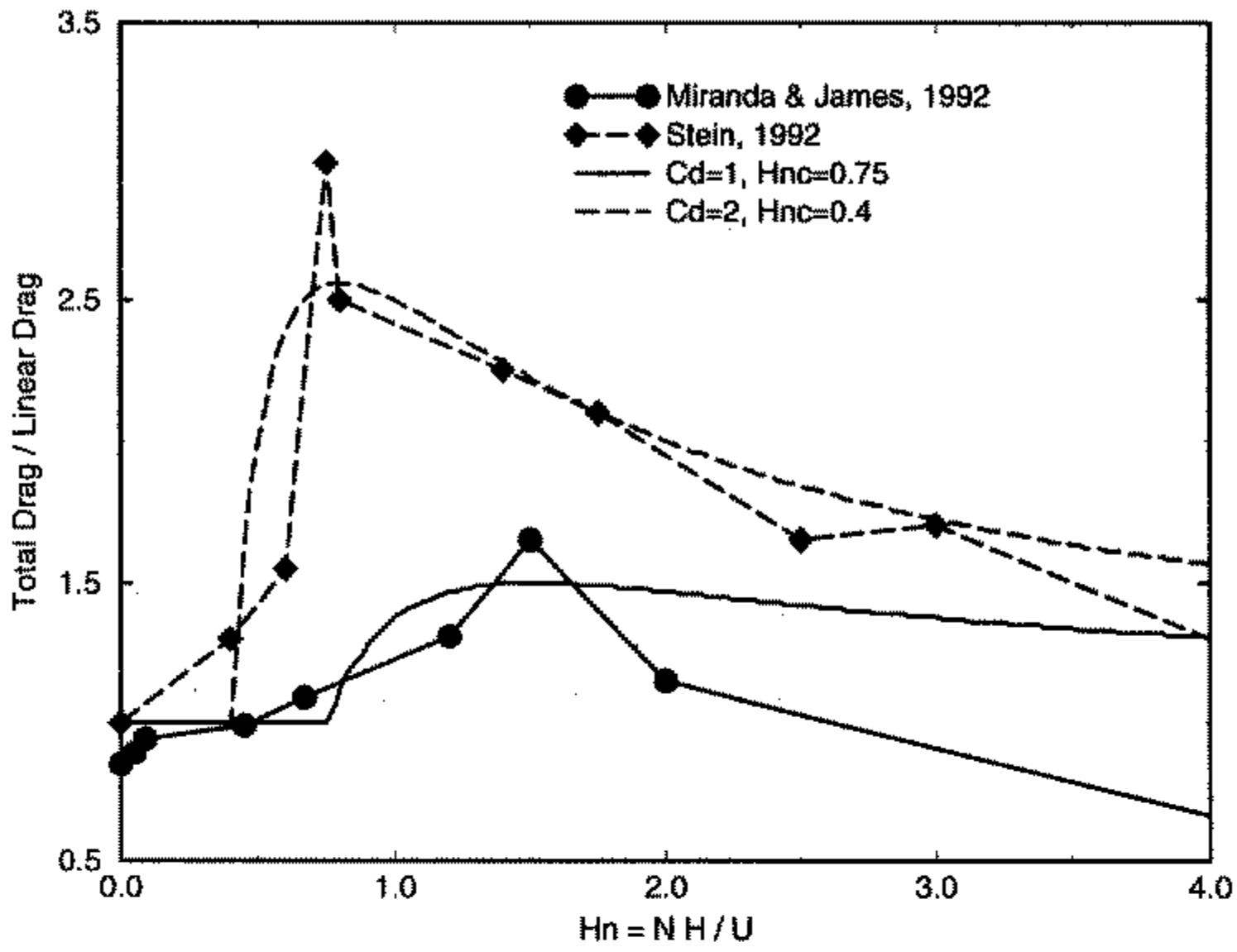

Figure 2. Ratio between the total mountain drag and the linear gravity-wave drag as a function of H_n. The continuous line and the dotted line correspond to the drag ratio predicted by the conceptual model upon which the new subgrid-scale orographic drug scheme is based. The dotted line with diamond symbols corresponds to values found in 2-D nonlinear simulations (Stein 1992). The continuous line with circle symbols correspond to values found in 3-D nonlinear simulations (Miranda and James 1992).

upstream blocking. Three-dimensional drag values are approached by this conceptual model for $C_d = 1$, $H_{nc} = 0.75$. In this case, the smaller value of C_d is probably related to the reduction of upstream blocking in three-dimensional simulations. A larger H_{nc} corresponds to a reduction of the nonlinear effects due to the three-dimensional dispersion of the mountain waves. In the new scheme, proposed below, these effects will be partly taken into account by allowing the value of C_d to vary with the aspect ratio of the obstacle, as in the case of separated flows around immersed bodies (Landweber 1961), while at the same time setting the critical number H_{nc} equal to 0.5 as a constant intermediate value. Note also that for large H_n, Eq. (8) overestimates the drag in the three-dimensional case, because the flow dynamics become more and more horizontal, and the incidence of gravity waves is diminished accordingly. In the scheme a reduction of this kind in the mountain-wave stress could have been introduced by replacing the mountain height given in Eq. (3) with a lower 'cut-off' mountain height, $H(H_{nc}/H_n)$. Nevertheless, this has not been done in the new parametrization scheme partly because a large non-dimensional mountain height often corresponds to slow flows for which the drag given by Eq. (8) is then, in any case, very small.

3. Description of the new scheme

The above ideas have been applied to represent the effects of SSO in the ECMWF model. Following Baines and Palmer (1990), the SSO over one gridpoint region (GPR) is represented by four parameters μ, γ, σ and θ which stand for the standard deviation, the anisotropy, the slope and the geographical orientation of the orography, respectively. These four parameters have been calculated from the US Navy (USN) ($10' \times 10'$) data-set (see appendix for details).

The scheme uses values of low-level wind velocity and static stability which are partitioned into two parts. The first part corresponds to the incident flow which passes over

the mountain top, and is evaluated by averaging the wind, the Brunt–Väisälä frequency and the fluid density between μ and 2μ above the model mean orography. Following Wallace *et al.* (1983), 2μ is interpreted as the envelope, of the subgrid-scale mountain peaks above the model orography. The wind, the Brunt–Väisälä frequency and the density of this part of the low-level flow will be labelled U_H, N_H and ρ_H, respectively. The second part is the 'blocked' flow, and its evaluation is based on a very simple interpretation of the non-dimensional mountain height H_n. To first order in the mountain amplitude, the obstacle excites a wave, and the sign of the vertical displacement of a fluid parcel is controlled by the wave phase. If a fluid parcel ascends the upstream mountain flank over a height large enough to significantly modify the wave phase, its vertical displacement can become zero, and it will not cross the mountain summit. In this case, the blocking height, Z_b, is the highest level located below the mountain top for which the phase change between Z_b and the mountain top exceeds a critical value H_{nc}, i.e.

$$\int_{Z_b}^{3\mu} \frac{N}{U_p}\, dz \geqslant H_{nc}. \tag{9}$$

In the inequality (9), the wind speed, $U_p(z)$, is calculated by resolving the wind, $U(z)$, in the direction of the flow U_H. Then, if the flow veers or backs with height, (9) will be satisfied when the flow becomes normal to U_H. Levels below this 'critical' altitude define the low-level blocked flow. The inequality (9) will also be satisfied below inversion layers, where the parameter N is very large. These two properties allow the new parametrization scheme to mimic the vortex shedding observed when pronounced inversions occur (Etling 1989). The upper limit in the inequality (9) was chosen to be 3μ, which is above the subgrid-scale mountain tops. This ensures that the integration in inequality (9) does not lead to an underestimation of Z_b, which can occur because of the limited vertical resolution when using 2μ as an upper limit (a better representation of the peak height), but this upper limit could be relaxed given better vertical resolution.

In the following subsection the drag amplitudes will be estimated, combining formulae valid for elliptical mountains with real orographic data. Considerable simplifications are implied and the calculations are, virtually, scale analyses relating the various amplitudes to the SSO parameters. Hence, the calibration and validation of the new scheme, described in sections 4 and 5, are essential.

(*a*) *The blocked-flow drag*

Within a given layer located below the blocking level Z_b, the drag is given by Eq. (5). At a given altitude z, the intersection between the mountain and the layer approximates to an ellipse of eccentricity

$$(a', b') \approx (a, b)\left(\frac{Z_b - z}{z + \mu}\right)^{1/2}, \tag{10}$$

where, by comparison with Eq. (6), it is also supposed that the level $z = 0$ (i.e. the model mean orography) is at an altitude μ above the mountain valleys. If the flow direction is taken into account, the length $l(z)$ can be written approximately as

$$l(z) \approx 2\max(b\cos\psi, a\sin\psi)\left(\frac{Z_b - z}{z + \mu}\right)^{1/2} \tag{11}$$

where ψ is the angle between the incident flow direction and the normal ridge direction, θ. For one GPR, and uniformly distributed SSO, if the incident flow is normal to the ridge

($\psi = 0$), it encounters $L/2a$ obstacles, whereas if it is parallel to the ridge ($\psi = \pi/2$) it encounters $L/2b$ obstacles, where L is the length scale of the GPR. If we sum up these contributions, the dependence of Eq. (11) on a and b can be neglected, and the length $l(z)$ becomes

$$l(z) = L\left(\frac{Z_b - z}{z + \mu}\right)^{1/2}. \tag{12}$$

Furthermore, the number of consecutive ridges (i.e. located one after the other in the direction of the flow) depends on the obstacle shape: there are approximately $L/2b$ successive obstacles when the flow is along the ridge, and $L/2a$ if it is normal to the ridge. If we take this into account, together with the flow direction, then

$$l(z) = \frac{L^2}{2}\left(\frac{Z_b - z}{z + \mu}\right)^{1/2} \max\left(\frac{\cos\psi}{a}, \frac{\sin\psi}{b}\right). \tag{13}$$

Relating the parameters a and b to the SSO parameters $a \approx \mu/\sigma$ and $a/b \approx \gamma$, and allowing the drag coefficient to vary with the aspect ratio of the obstacle as seen by the incident flow, we have

$$r = \frac{\cos^2\psi + \gamma \sin^2\psi}{\gamma \cos^2\psi + \sin^2\psi} \tag{14}$$

the drag per unit area and per unit height can be written

$$\mathbf{D}_b(z) = -C_d \max\left(2 - \frac{1}{r}, 0\right) \rho \frac{\sigma}{2\mu}\left(\frac{Z_b - z}{z + \mu}\right)^{1/2} \max(\cos\psi, \gamma \sin\psi)\frac{\mathbf{U}|\mathbf{U}|}{2}. \tag{15}$$

The drag coefficient is modulated by the aspect ratio of the obstacle to account for the fact that C_d is twice as large for flow normal to an elongated obstacle as it is for flow round an isotropic obstacle; this is indicated by the results shown in Fig. 2. The drag tends to zero when the flow is nearly along a long ridge because flow separation is not expected to occur for a configuration of that kind. It can be shown that the term $\max(\cos\psi, \gamma \sin\psi)$ is similar to a later form used for the directional dependence of the gravity-wave stress. For simplicity, this later form has been adopted; i.e.

$$\mathbf{D}_b(z) = -C_d \max\left(2 - \frac{1}{r}, 0\right) \rho \frac{\sigma}{2\mu}\left(\frac{Z_b - z}{z + \mu}\right)^{1/2} (B \cos^2\psi + C \sin^2\psi)\frac{\mathbf{U}|\mathbf{U}|}{2} \tag{16}$$

where the constants $B(\gamma)$ and $C(\gamma)$ are defined below. The difference between Eq. (15) and Eq. (16) has been shown to have only a negligible impact on all aspects of the model's behaviour.

In practice, Eq. (16) is suitably resolved and applied to the component form of the horizontal momentum equations. This equation is applied level by level below Z_b and, to ensure numerical stability, a quasi-implicit treatment is adopted whereby the wind velocity $\mathbf{U}$ in Eq. (16) is evaluated at the updated time $t + \mathrm{d}t$, while the wind amplitude, $|\mathbf{U}|$, is evaluated at the previous time step.

(*b*) *The gravity-wave drag*

This gravity-wave part of the scheme is based on the work of Miller *et al.* (1989) and Baines and Palmer (1990), and takes into account some three-dimensional effects in the wave stress amplitude and orientation. For clarity and convenience, a brief description is

given here. On the assumption that the SSO has the shape of one single elliptical mountain, the mountain wave stress can be written as (Phillips 1984)

$$(\tau_1, \tau_2) = \rho_H U_H N_H H^2 b G(B \cos^2 \psi_H + C \sin^2 \psi_H, (B - C) \sin \psi_H \cos \psi_H) \quad (17)$$

where $B = 1 - 0.18\gamma - 0.04\gamma^2$; $C = 0.48\gamma + 0.3\gamma^2$; G is a constant of order unity. Furthermore, when b or a are significantly smaller than the length L, characteristic of the gridpoint region size, there are, typically, $L^2/4ab$ ridges inside the GPR. Summing all the associated forces we find the stress per unit area, viz.

$$(\tau_1, \tau_2) = \rho_H U_H N_H \mu\sigma G\{B \cos^2 \psi_H + C \sin^2 \psi_H, (B - C) \sin \psi_H \cos \psi_H\} \quad (18)$$

where H has been replaced by 2μ, and a by μ/σ.

It is worth noting that, since the basic parameters ρ_H, U_H, N_H are evaluated for the layer between μ and 2μ above the mean orography that defines the model's lower boundary, there will be much less diurnal cycle in the stress than in previous formulations that used the lowest model levels for this evaluation. The vertical distribution of the gravity-wave stress will determine the levels at which the waves break and slow down the synoptic flow. Since this part of the scheme is active only above the blocked flow, this stress is now constant from the bottom model level to the top of the blocked flow, Z_b. Above Z_b, up to the top of the model, the stress is constant until the waves break. This occurs when the total Richardson number, Ri, falls below a critical value Ri_c, which is of order unity. When the non-dimensional mountain height is close to unity, this algorithm will usually predict wave breaking at relatively low levels; this is not surprising since the linear theory of mountain gravity waves predicts low-level breaking waves at large non-dimensional mountain heights (Miles and Huppert 1969). In reality, the depth over which gravity-wave breaking occurs is more likely to be related to the vertical wavelength of the waves. For this reason, when low-level wave breaking occurs in the scheme, the corresponding drag is distributed (above the blocked flow), over a layer of thickness ΔZ, equal to a quarter of the vertical wavelength of the waves, i.e.

$$\int_{Z_b}^{Z_b+\Delta Z} \frac{N}{U_p} \, dz \approx \frac{\pi}{2}. \quad (19)$$

Above the height $Z_b + \Delta Z$ are waves with an amplitude such that $Ri > Ri_c$.

4. Off-line calibration

The new scheme depends essentially on the four parameters, C_d, G, Ri_c and H_{nc}. The first two directly control the amplitude of the blocked-flow drag and of the gravity-wave drag. The third and fourth parameters control the vertical distribution of these drags. The final forms of inequality (9) and Eqs. (16) and (18) contain several assumptions and simplifications; therefore, before testing the scheme in the model, investigations of the sensitivity of parameter values have been made. This was done using an off-line calibration in which the SSO scheme is just a predictor of the perpendicular component of the mountain pressure drag, and of the momentum flux vertical profiles which were observed during the two-month-long PYREX field experiment.

In the following, the incident wind and temperature (extracted from the ECMWF reanalysis (Lott 1995) of the data collected during the PYREX campaign (Bougeault *et al.* 1993)) are provided every six hours, thus giving 240 pairs as input field to the new parametrization. For each flow profile the parametrization scheme is used to calculate a

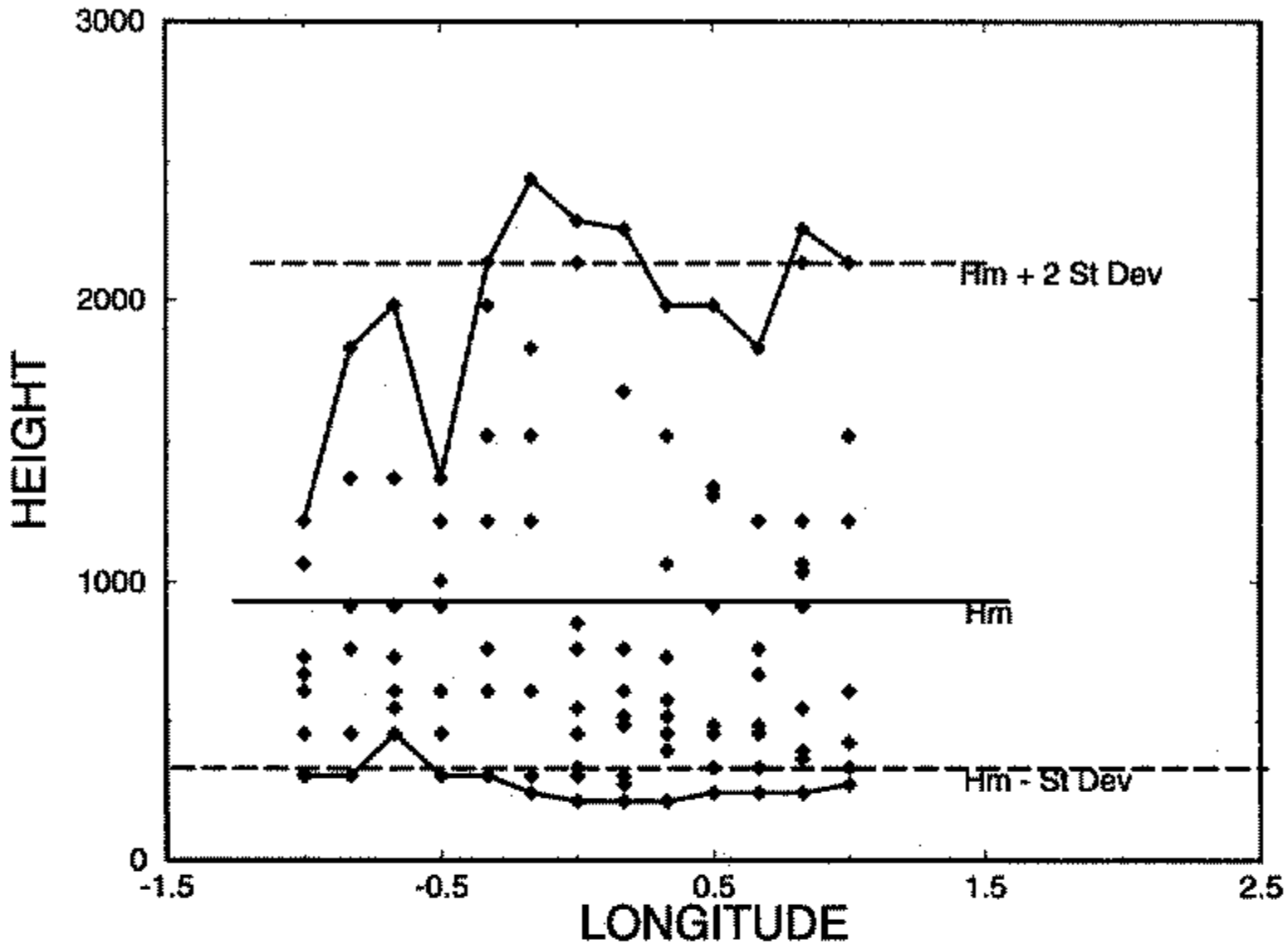

Figure 3. The US Navy orography data-set ($10' \times 10'$) of mountain elevations plotted as a function of longitude for a gridpoint region covering the Pyrenees mountain range between longitudes $-1°$W, $1°$E and latitudes $41.7°$N, $43.3°$N.

mountain drag and a momentum profile averaged over a grid-box area. In the ECMWF model at truncation T106, a typical GPR has the size of the whole Pyrenees. Off line, the GPR can be chosen to cover the area bounded by longitudes $-1°$W, $1°$E and latitudes $41.7°$N, $43.3°$N, which contains most of the massif and which is centred on the PYREX central transect. Over this area, the ($10' \times 10'$) USN data-set provides 110 values of the orography elevation. These data are displayed in Fig. 3 as a function of their longitude. On this figure only 101 values are indicated because, in the USN data-set, some adjacent values are identical. Although this indicates a need for a better orographic data-set, the representation of the Pyrenees in the USN data-set was found to be good enough to justify the following comparison. Over the GPR, the SSO parameters have values, $\gamma = 0.63$, $\sigma = 0.0021$, $\theta = 75°$, and h_m (the model orographic height) $= 930$ m. The values of γ and θ seem realistic. The slope parameter, σ, seems rather small, and this underestimation is related to the rather poor resolution of the data-set. In Fig. 3 the values $h_m + 2\mu$ and $h_m - \mu$ are also indicated. As mentioned earlier, this example illustrates that the envelope of the peaks corresponds well to $h_m + 2\mu$, while the envelope of the valleys is approximated by $h_m - \mu$. The total subgrid-scale mountain height is then 3μ, approximately equal to 1800 m, which is a good estimate of the Pyrenees elevation. It is smaller than the mountain elevation measured along the PYREX microbarographs transect (i.e. approx 2100 m), which is not surprising since the GPR contains the central transect, but also covers that part of the Pyrenees which is significantly lower than the central maximum. It can therefore be assumed that the line-averaged pressure drag, measured along the central transect, will overestimate the area-averaged pressure drag of the entire massif as estimated by the scheme. To quantify this overestimation, it is assumed that the pressure drag measured along one given north–south transect located at a given longitude, φ, has the order of magnitude, $NUH^2(\varphi)$. Here H stands for the maximum mountain height at longitude φ. This predictor of the measured pressure drag, according to Bessemoulin *et al.* (1994), was found to perform well along the Greenwich meridian ($\varphi = 0$). In this case, an estimation

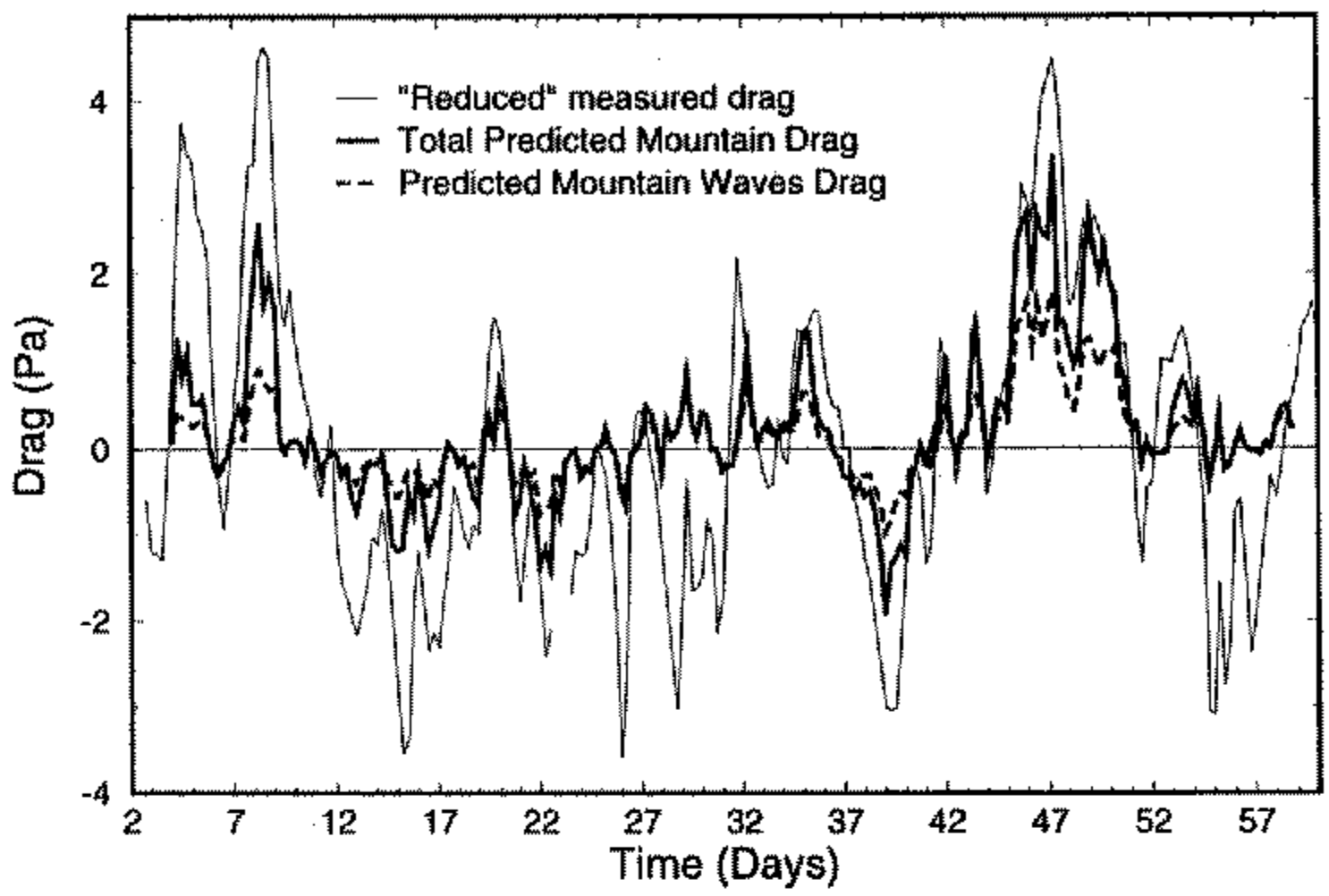

Figure 4. Off-line calibration: comparison between the pressure drag measured during the PYREX field experiment and the drag predicted by the new scheme. The comparison is made every six hours, during the two months of the PYREX campaign.

of the north–south component of the stress per unit area of the Pyrenees is

$$\tau_{\text{reduced}} = \frac{1}{\varphi_2 - \varphi_1} \int_{\varphi_1}^{\varphi_2} NU H^2(\varphi)\ \mathrm{d}\varphi \approx \frac{\overline{H^2}}{H^2(0)} D_{\text{measured}}, \tag{20}$$

later referred to as the reduced measured stress. This ratio between the measured drag and the stress to be parametrized over the GPR can be estimated using the USN data-set, giving the mountain drag per unit area over the GPR as, approximately, 75% of the drag measured along the PYREX central transect.

Figure 4 shows the comparison between the drag predicted by the SSO scheme and the reduced measured drag; also shown is the gravity-wave drag contribution to the overall parametrized mountain drag. The parameters of the scheme in this case are, $C_d = 1$, $G = 0.5$, $H_{nc} = 0.5$, $Ri_c = 1$. This set of parameters was chosen to give a satisfactory compromise between the forecast performance of the model at T106 and the PYREX data. Figure 4 shows that in many cases the new scheme gives a drag which is realistic in sign and in amplitude. The maxima and the minima of the measured drag are generally well represented by the scheme. Nevertheless, there are two periods during which the scheme is inadequate (days 27–31 and 54–59). These periods are marked by strong westerly winds, when the measured drag is mainly a 'lift' force, which is not parametrized in the new scheme. Figure 4 also shows that the contribution of the blocked-flow drag to the total mountain drag is significant when compared with the contribution from the gravity-wave drag. On many dates (days 4–6, 7–9, 14.4–15.5, 22–23, 33–35, 38.5–40.5, 43–44, 45–50) the drag contribution from the low-level blocked flow significantly enhances the predicted mountain drag, bringing it closer to the measured drag.

The same off-line procedure has been applied to the gravity-wave drag scheme previously used (until replaced by this new one), and the results are displayed in Fig. 5. In the previous scheme a constant k is defined that relates the amplitude of the gravity-wave stress to a typical horizontal wavelength of the orographic disturbance (Palmer *et al.* 1986). With the value of k equal to 2.5×10^{-5} m^{-1}, Fig. 5 shows that the old scheme gives too small a drag. This would correspond to an overestimation of the typical horizontal wavelength of the disturbance (noted by these authors). Following Bougeault *et al.* (1993), multiplying

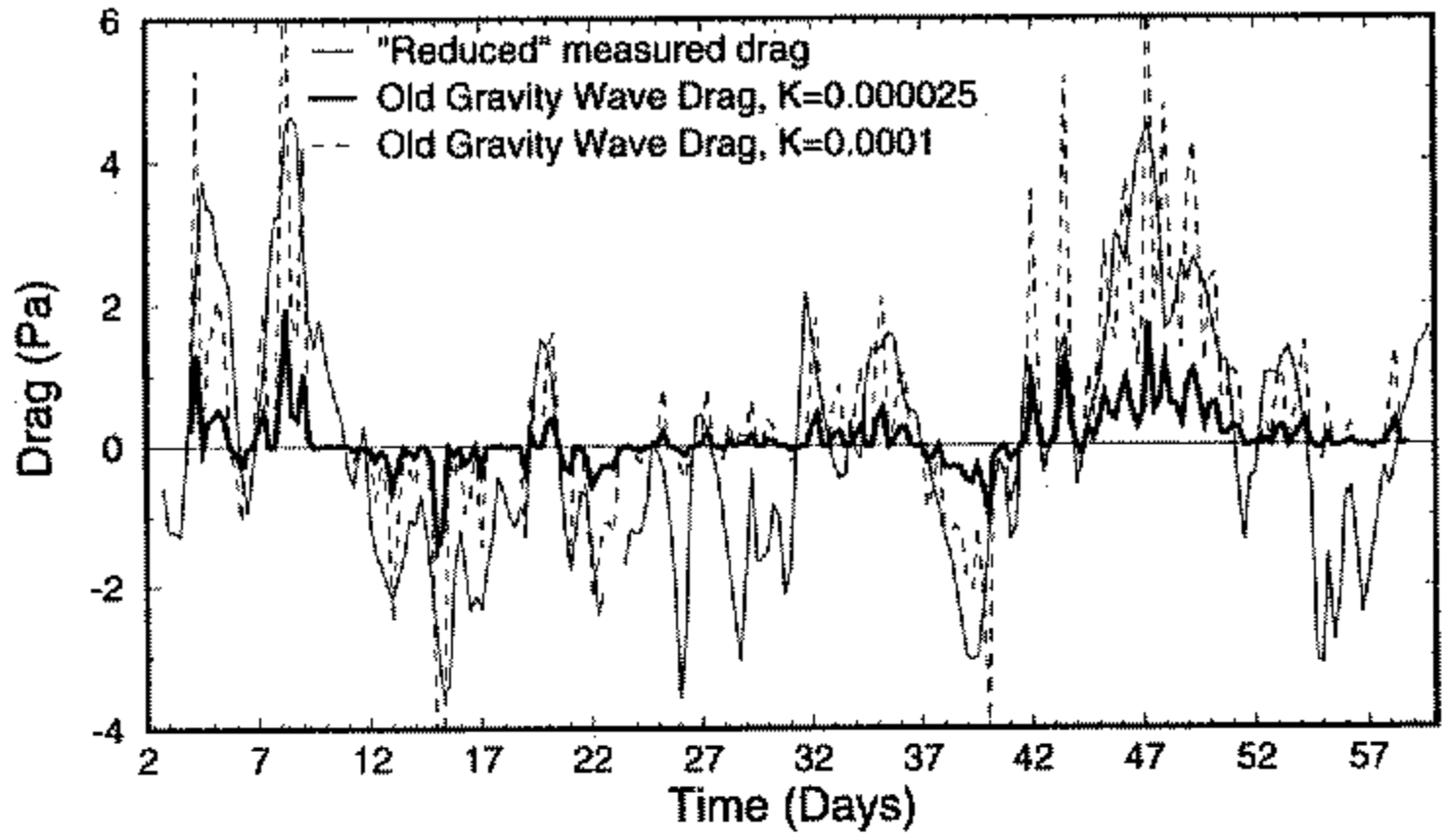

Figure 5. Same as Fig. 4 but for the old gravity-wave drag scheme. The dashed line ($k = 0.000\,025\ \mathrm{m}^{-1}$) shows the operational gravity-wave drag scheme. The dotted line ($k = 0.0001\ \mathrm{m}^{-1}$) shows the same operational scheme but for a larger value of the constant k.

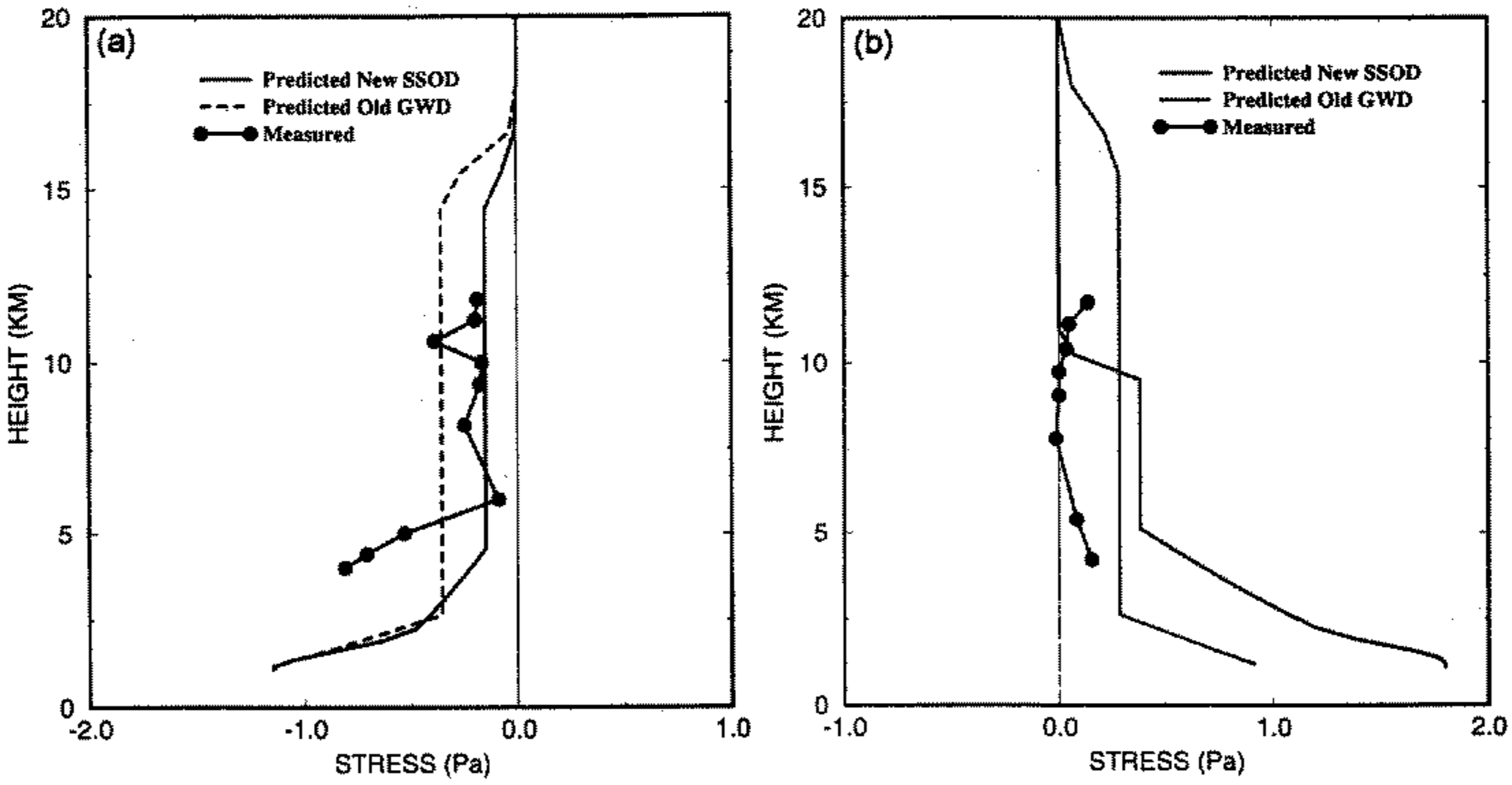

Figure 6. Off-line calibration: stress vertical profiles predicted by the new scheme, by the old gravity-wave drag scheme and as measured. (a) 6 UTC 15 October 1990, (b) 6 UTC 16 November 1990.

k by 4, i.e. $k = 1.0 \times 10^{-4}\ \mathrm{m}^{-1}$, leads to a far better agreement with the observations. Nevertheless, even in this configuration, the scheme still shows only moderate skill. A strong diurnal cycle is present which is unrealistic. This diurnal cycle is a result of using only the three lowest model levels to estimate the characteristics of the incident flow in the old scheme. Very large amplitude drags occur in the morning, when there is considerable low-level stability, and very small amplitude drags in the late afternoon, when the static stability is near neutral.

Figure 6(a) shows the horizontal momentum flux vertical profiles generated by the new scheme, by the old scheme, and from the measurements for 15 October 1990 at 6 UTC (Bougeault, personal communication). At low levels, below about 2100 m, the stress profile

shows a strong shear which is related to the drag of the blocked flow. Above this layer, up to about 4500 m, the stress profile shows a shear related to low-level breaking gravity waves. It is important to note that this shear extends significantly above the mountain top, in qualitative agreement with the low-level shear stress observed during aeroplane flights between 3900 m and 5700 m. Such an 'elevated' low-level shear stress does not occur in the old scheme. The vertical stress profile in the new scheme was found to be rather sensitive to the value of the critical Richardson number, Ri_c, since it controls the amount of gravity-wave activity that is transmitted to higher levels. According to linear stability theory, it should be 0.25 (Miles 1961; Howard 1961) but observations (Woods 1969), and some nonlinear investigations (Abarbanel *et al.* 1986), suggest that a stratified shear flow can be unstable when the minimum Richardson number is of order unity. At small Ri_c, e.g. around 0.25, the scheme predicts that most of the wave drag is at high altitudes, and that little low-level 'breaking-wave' drag occurs. The value $Ri_c = 1$ was, therefore, adopted (Fig. 6), for which value the scheme predicts significant low-level wave drag. It also predicts that the stress decreases with height to a value which fits reasonably well with the stress value as measured above 6000 m during the aeroplane flights. More profiles are shown in Fig. 6(b) for 16 November 1990 at 6 UTC. Here again the new scheme shows strong low-level drag contributions from the blocked-flow drag and breaking gravity waves. At high levels in these particular examples both the old and new schemes have stresses that are too large. However, it was assumed that area-averaged momentum flux is comparable to the line-averaged values measured above the central transect. This hypothesis is known to be questionable since significant differences in line-averaged profiles often occur for different two-dimensional vertical cross-sections located close to one another (Hoinka and Clark 1991). Nevertheless, as momentum fluxes were measured along only one transect during PYREX, such differences were not evaluated. It is also noteworthy that the stress decrease observed just above the mountain tops can be due to partially trapped non-hydrostatic gravity waves. Those waves were often observed during PYREX. Although the same stress decay with altitude can also indicate wave breaking, as is assumed to be the case in the new scheme, it is possible that the predicted stress matches the data for the wrong reasons. The 'wave-breaking' hypothesis was, nevertheless, adopted because of the large uncertainties about the amount of mountain-drag due to trapped waves. With such limitations in mind, these momentum-flux comparisons can indicate only qualitative agreement between the scheme and the measurements.

5. VERIFICATION AND DIAGNOSTICS

(*a*) *On-line verification*

Although useful and straightforward to do, the preceding calibration does not guarantee that the new scheme will behave properly near the Pyrenees in forecast configurations. In this section, that behaviour is examined with the ECMWF model at both T106 and T213 resolutions. The tests, in which the model orography is a mean orography, will show that the low-level blocked-flow drag more than compensates for the envelope orography. Attention is limited to the PYREX period of intense observations (PIO), which covers 25% of the two months of the PYREX campaign, during which the wind component normal to the mountain range was often large. This limits the on-line verifications to 60 out of the 240 cases defined in section 4. The procedure followed is close to that due to Lott (1995) in which the model transect was as close as possible to the PYREX transect. In the ECMWF model, the transect is defined along the Greenwich meridian, making its orientation slightly different from that of the PYREX transect which was oriented at right-angles to the ridge. Although this difference could be handled by suitable interpolation of the data in the model, making

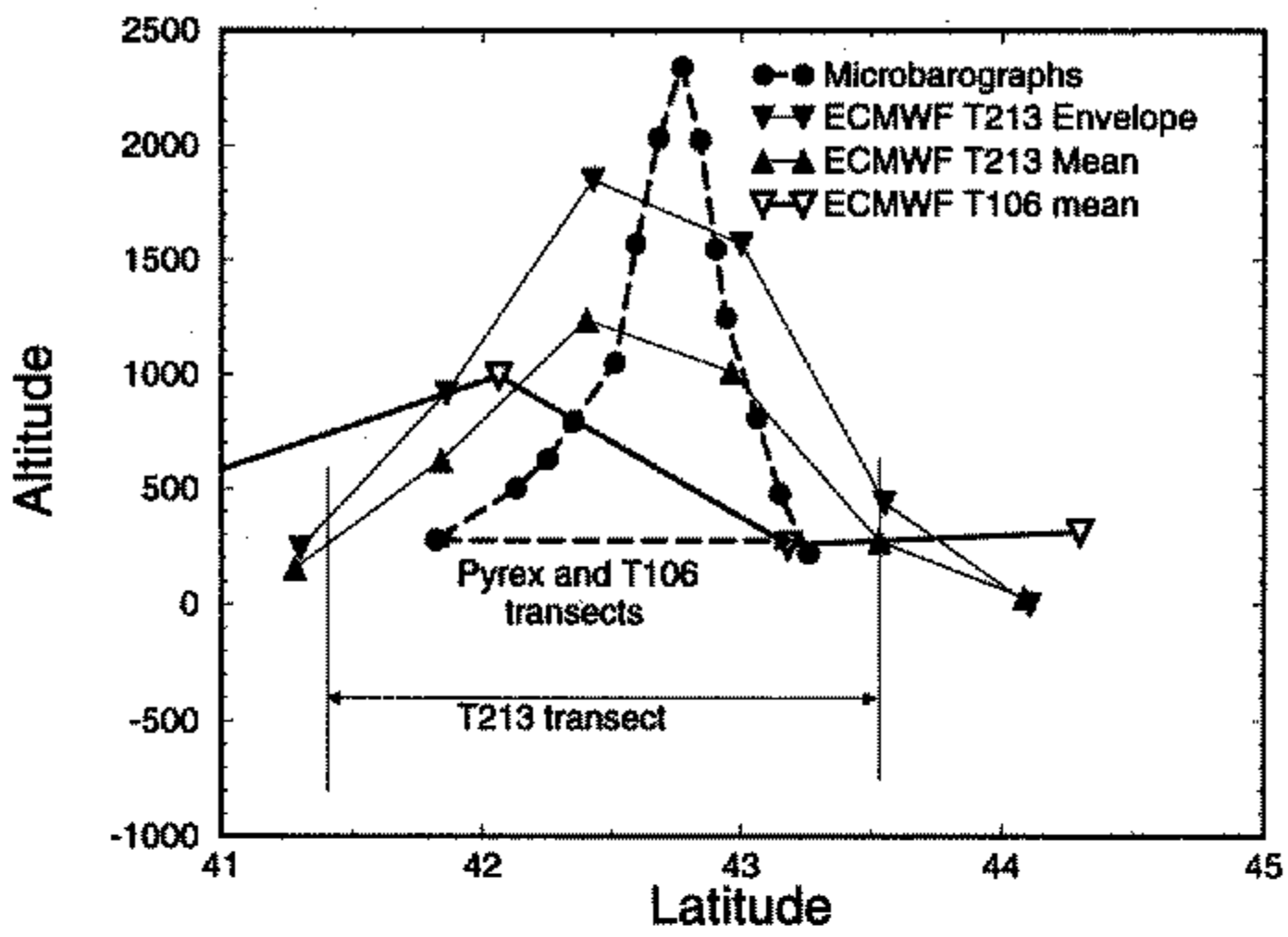

Figure 7. Orography profiles of the transects along which the different drags are calculated.

such a correction was found to have a small impact on the results. These different transects are shown in Fig. 7. Since the Pyrenees are quite well represented in the model at T213, the length of the transect in the model was taken a little larger than the PYREX transect to try to capture, as much as possible, a model pressure drag that could be related to the Pyrenees. As Fig. 7 shows, 5 gridpoints along the Greenwich meridian are necessary to define the transect at T213. At T106, the Pyrenees are very difficult to identify, in which case the mountain drag has to be entirely parametrized. At this lower truncation, it can be seen that the PYREX transect is almost entirely located between two gridpoints of the model. As a consequence, the drag due to the Pyrenees in the T106 model will be taken to be the mean of the subgrid-scale orographic drag between these two gridpoints, with the mountain drag interpreted as the sum of the contribution of the boundary-layer turbulence scheme and the subgrid-scale orographic drag. This might seem surprising since the microbarographs were separated by a distance of, typically, 10 km along the PYREX transect and could not capture pressure drag related to turbulence with horizontal scales significantly smaller than this. On the other hand, it is clear that the new scheme and the boundary-layer scheme will interact at low levels. The state of knowledge concerning turbulence above high and narrow mountains is poor, both theoretically and as regards measurements. With such uncertainties, it is reasonable to suppose that the total mountain drag (i.e. the model pressure drag + the boundary-layer drag + a new subgrid-scale orography drag) should be at least as large as the measured pressure drag. The role of the boundary layer in this context has been discussed at greater length by Lott (1995).

Figure 8 shows the T106 model drag (from forecasts run for the equivalent of 48 hours with data extracted every 6 hours) compared to the 'reduced' measured drag for the 60 cases defined above. The parametrized stress does well during most of the normal ridge configurations. A similar comparison between drags predicted by the forecast model and the old gravity-wave drag scheme did not show such skill.

In T213 forecast configurations, the parametrized drags make up the difference between the model pressure drag and the measured pressure drag. With mean orography the model pressure drag is significantly smaller than it is in the operational model with envelope orography. This is simply related to the fact that, with the mean orography, the

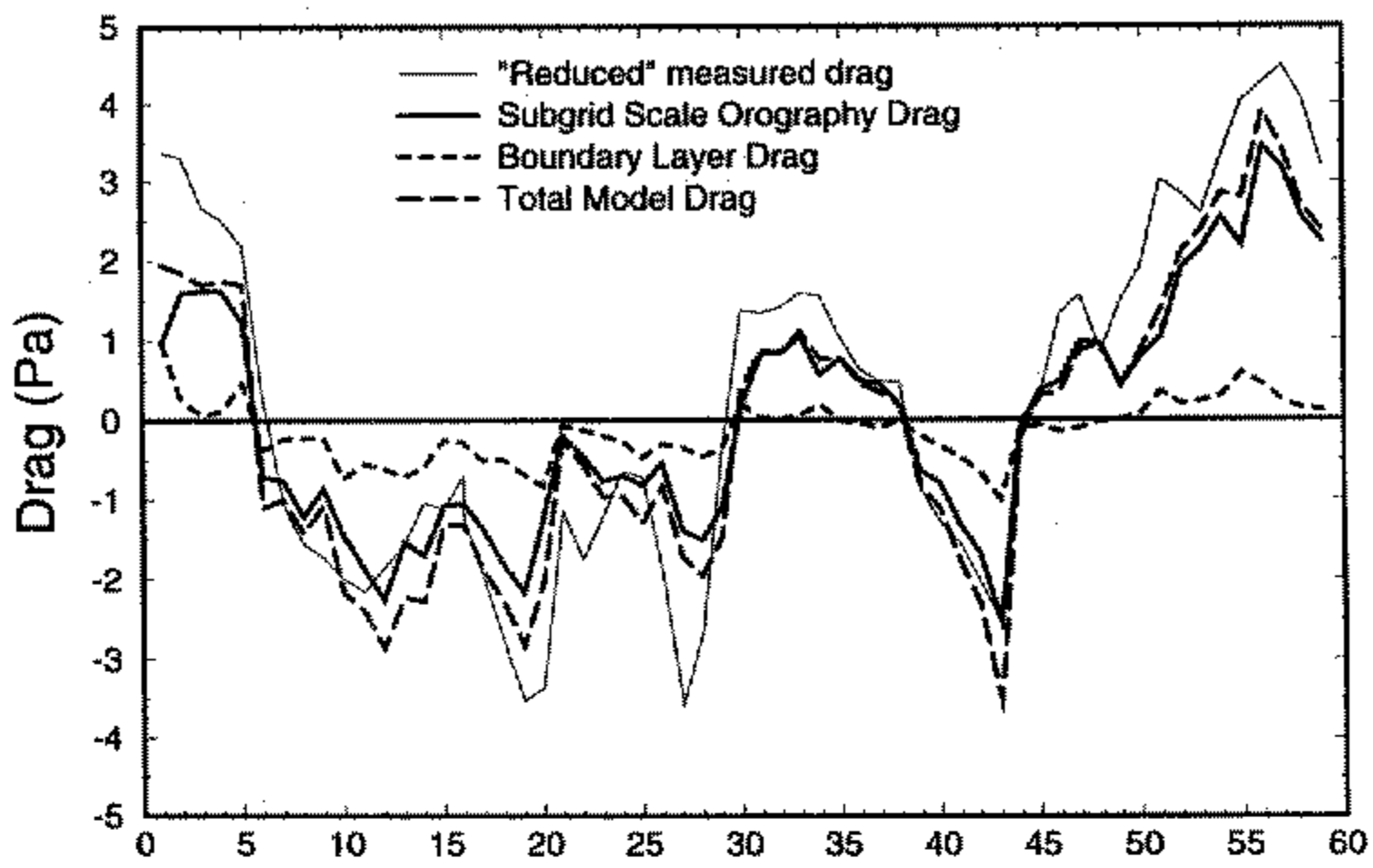

Figure 8. T106 forecasts: ECMWF model with mean orography and the new subgrid-scale orographic drag scheme. Parametrized mountain drags during PYREX. The comparison is limited to the 60 PIO cases defined in the text.

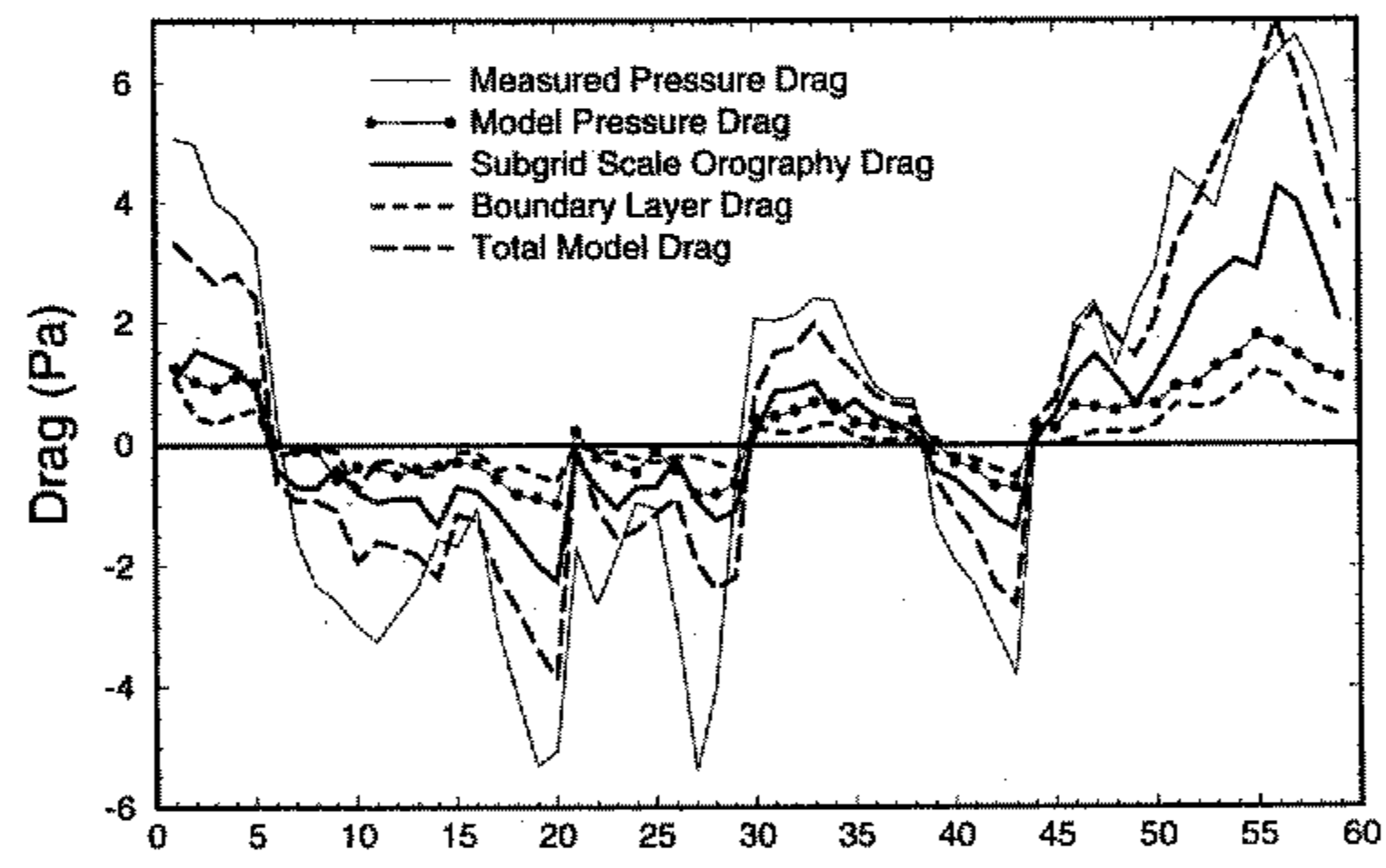

Figure 9. T213 forecasts: ECMWF model with mean orography and the new subgrid scale orographic drag scheme. Explicit model pressure drag and parametrized mountain drags during PYREX. The comparison is limited to the 60 PIO cases defined in the text.

maximum mountain height of the Pyrenees is significantly smaller than in the operational model with an envelope orography. In fact, Lott (1995) has shown that the model drag in the model is well estimated by the quantity NVH^2 where V is the wind component normal to the ridge. Since the explicit pressure drag is much reduced in the model with mean orography, the new scheme has to make a substantially larger contribution to the model mountain drag than was the case for the old gravity-wave drag when the envelope orography was used. Figure 9 shows that this is the case during all the PYREX POIs. While the old gravity-wave drag is very small and does not make up the difference often observed between the model drag and the measured drag, the new orography representation of the subgrid-scale orography gives a parametrized drag that is large, and makes up the difference between the model pressure drag and the measured pressure drag in a very consistent way.

(*b*) *Case-study*

In the new scheme, we consider that when the flow component normal to the ridge is large, the mountain drag is related mainly to a slowing down of the low-level flow and to upward-propagating waves. The amplitude of the wave stress significantly above the mountain top is often small (when compared to the surface stress) because high mountains generate waves which very often break close to the mountain top. These mechanisms result in a large low-level drag which can have a significant impact on the flow dynamics at the subsynoptic scale. The realism of the new scheme can therefore be evaluated by making diagnostics of the low-level flow in the model and comparing it with more accurate simulation of the flow near the Pyrenees. One case is examined, using isentropic diagnostics similar to that presented by Lott (1995). The impact of the scheme on the flow dynamics is studied by comparing a forecast in which the scheme is active with one in which it is not, both schemes having mean orography. Figure 10 presents such flow diagnostics on the surface $\theta = 293$ K. At this level, the synoptic flow is essentially from the north-west (Fig. 10(a)). Over the mountains, it is deflected significantly southward, and in the lee of the ridge the wind is significantly decelerated. Figure 10(b) shows the elevation of this isentropic surface, ranging from about 1700 m above the model ground upstream of the mountain, and descending to 1100 m south of the mountain. Although significantly distorted, this layer is at an altitude which experiences the low-level drag in the new scheme. The impression that the flow is decelerated at this level is reinforced by the presence of a vorticity dipole which begins over the mountain and extends quite far downstream (Fig. 10(c)). Nevertheless, the presence of this dipole can be due to a conversion of planetary vorticity into relative vorticity by changes in the isentropic layer depth, while conserving potential vorticity. In that case the occurrence of the vorticity dipole would depend essentially on reversible processes related to the advection by the flow of the potential vorticity. To evaluate whether this reversible picture applies here, we make use of the Bernoulli function (Fig. 10(d)),

$$B = c_p T + gz + \frac{u^2 + v^2}{2} \tag{21}$$

which, in the absence of body forces and diabatic heating, is a quantity that is conserved on isentropic surfaces (Schär 1993). The Bernoulli function shows a deficit across the ridge, since the flow essentially crosses the Bernoulli 'contours' as it passes over the ridge. To verify that this deficit is related to the new scheme, Fig. 10(e) and (f) show the flux of absolute vorticity (Haynes and McIntyre 1986), and the contribution to this flux from the non-conservative body forces and diabatic heating, which are determined by the physical parametrization scheme of the model, i.e.

$$\mathbf{u}(\xi_{r\theta} + f) + \mathbf{k} \times \mathbf{F} - \mathbf{k} \times \dot{\theta} \frac{\partial \mathbf{u}}{\partial \theta} \tag{22}$$

where $\mathbf{u}$ and $\xi_{r\theta}$ are the isentropic wind and the isentropic relative vorticity respectively, f is the planetary vorticity, $\mathbf{F}$ and $\dot{\theta}$ represent the body force and the diabatic processes related to the parametrization schemes, respectively. Comparing Fig. 10(e) and (f), the non-advective contribution to the absolute vorticity flux is clearly large over the mountain. Likewise comparing Fig. 10(e) with the Bernoulli function map, deficit of the Bernoulli function (which is the stream function of the absolute vorticity flux (Schär 1993)) must be due to the parametrized processes. The fact that the new scheme has a predominant role in the production of the wake is further confirmed by looking at the non-conservative forcing when the new scheme is switched off. This is significantly smaller (Fig. 11(b)),

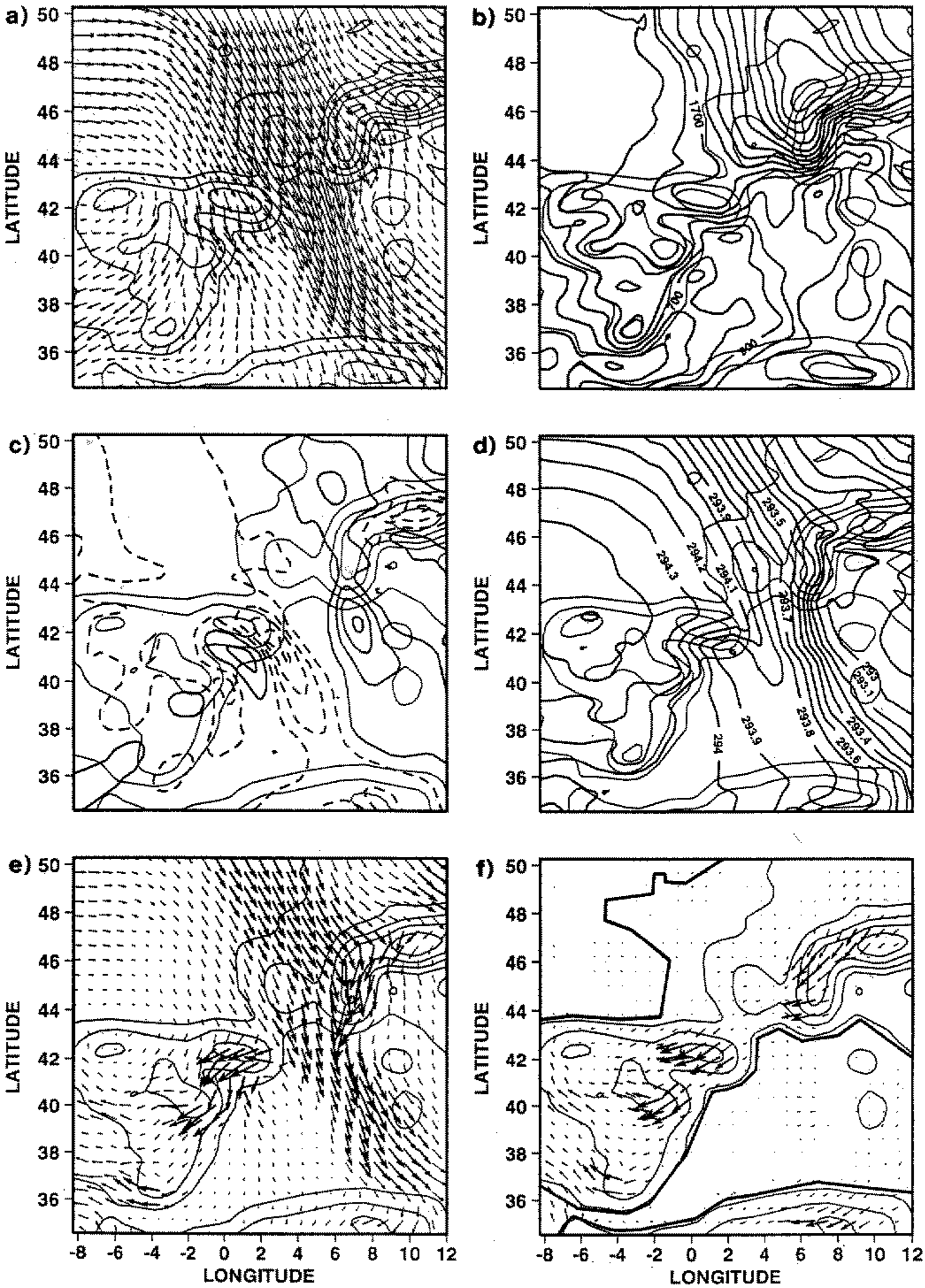

Figure 10. T213 forecast: ECMWF model with mean orography and the new subgrid-scale orographic drag scheme. 15 November 1990 at 6 UTC. Orography (interval: 400 m) and flow diagnostics on the isentropic surface $\theta = 293$ K. (a) wind; (b) height of isentropic surface, interval: 200 m; (c) isentropic relative vorticity, interval: 0.5×10^{-4} s^{-1}; (d) Bernoulli function, interval: 100 J kg^{-1}; (e) total potential vorticity flux; (f) potential vorticity fluxes due to the parametrized frictional forces and diabatic heating. Coastlines are shown on Fig. 10(f).

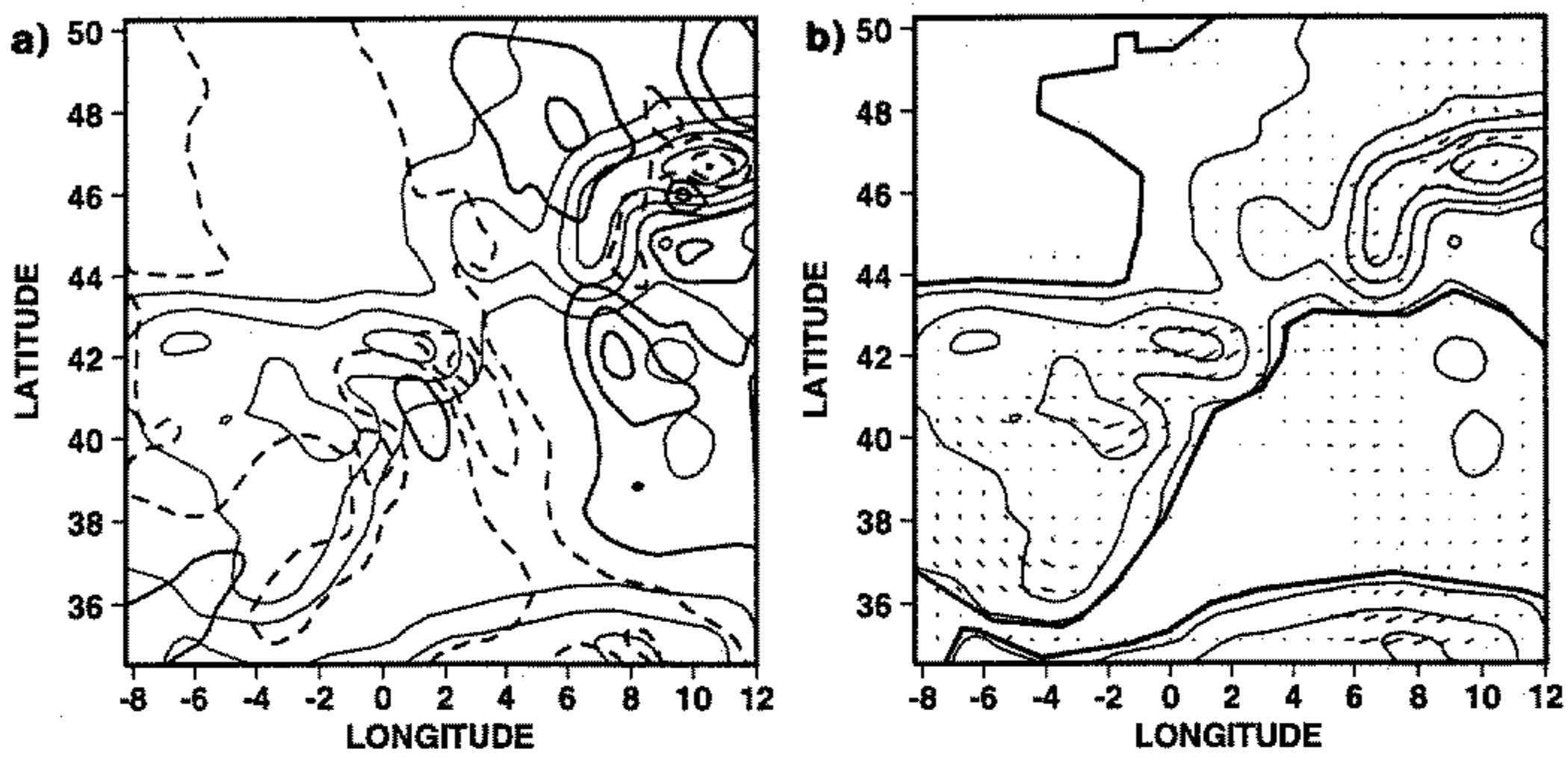

Figure 11. T213 forecast, ECMWF model with mean orography and no subgrid-scale orographic drag scheme. 15 November 1990 at 6 UTC. Orography (contour interval: 400 m) and flow diagnostics on the isentropic surface $\theta = 293$ K; (a) isentropic relative vorticity, interval: 0.5×10^{-4} s^{-1}; (b) potential vorticity fluxes due to the parametrized frictional forces and diabatic heating. Coastlines are shown on Fig. 11(b).

and the vorticity dipole is less pronounced (Fig. 11(a)). Lott (1995) has shown similar isentropic diagnostics of the mesoscale reanalysis of the PYREX data from the Peridot model (Bougeault and Mercusot 1992). In these diagnostics, a very similar wake was observed at this isentropic level, owing to flow separation processes occurring on the flanks of the Pyrenees.

6. Testing of the forecast performance

The preceding sections are intended to show that the new scheme is well based dynamically, and that it corresponds well with PYREX data diagnostics. However, a parametrization scheme in a global numerical model must perform well under a much wider range of situations. Furthermore, the ECMWF model is being routinely run at several horizontal resolutions ranging from T63 to T213. Consequently, extensive testing is required in such models before a new parametrization scheme can be considered suitable to replace an earlier one. Since different horizontal resolutions imply different basic orographies and different associated subgrid-scale orographic fields, the resolution issues are particularly prominent. In view of the PYREX testing at T106 and T213, and the fact that the current ECMWF operational system is run at T213, most of the forecast testing has been done at these higher resolutions. Results from T63 forecasts and longer simulations will not be dealt with here. As has been mentioned already, the new scheme is designed to be used together with a *mean* orography.

(*a*) *An 'effective' orography*

Since an envelope orography is substantially higher than the mean one to be used with the new SSO scheme proposed here, the question arises as to whether there is an 'effective' orography implied when using the new scheme, since it influences the flow well above the mean orographic heights. As presented here, the scheme directly affects

only the momentum, and not temperature or moisture variables. As such, the 'effective' orography for surface fluxes of heat and moisture, for example, is the (resolved) mean one. However, there is also an effect on these fluxes through the near-surface wind field which will be modified by the new scheme; this, however, is difficult to quantify. For the momentum there is the obvious impact of Z_b, the blocking height, but since the subgrid-scale orography also has a vertical profile (given by the square-root part of Eq. (16)), a possible better measure of 'effective' orography ought to be given by the equation

$$h_{\text{eff}}(x, y) = h_{\text{mean}}(x, y) + \delta h(x, y, t)$$

where

$$\delta h(x, y, t) = \int_0^{Z_b} \left(\frac{Z_b - z}{\mu + z} \right)^{1/2} \, dz$$

the integral being a function of both location and time. This integral can be evaluated analytically giving

$$\delta h = Z_b\{(\beta^2 + 1) \tan^{-1}(1/\beta) - \beta\}$$

where $\beta^2 = \mu / Z_b$. For $Z_b = \mu$, for example, $\delta h \approx 0.57\mu$.

Figure 12 shows an example of this orographic increment computed as a ten-day forecast average. Also shown is the corresponding mean orography. This 'effective' orography increment can be large (over a thousand metres for most major mountain ranges) and thus provides a higher 'effective' orography than a one standard-deviation envelope would.

(*b*) *Impact of the new parametrization*

(i) *Forecasts only.* One of the ways that the impact of the parametrization scheme can be assessed is to use objective skill scores. Ideally forecasts should be run from analyses generated with an assimilation system using the same model as the forecast one (see section 6(b)(ii)), however, to obtain a broad seasonal spread of initial dates, the scheme was first tested without reassimilation. Figure 13 shows comparisons of two sets of twelve forecasts (one per calendar month), run at T106 and T213, as measured by root-mean-square height errors. The comparison is between forecasts run with mean orography only, and forecasts with mean orography plus the new scheme. In general the impact of the scheme is positive. This is also true for tropical wind verification (not shown). There is, however, little impact in the case of the southern hemisphere.

Prior to operational implementation of this scheme, two three-week T213 assimilation and forecast experiments were carried out. For one experiment, the period 6 to 26 December 1994, the forecasts (only) were re-run with the orography scheme switched off, i.e. with mean orography only. This isolates the impact of the new scheme on the forecast model only. Figure 14 shows the root-mean-square 500 mb height errors averaged over the set of nineteen forecasts from 8 to 26 December 1994, from which the benefits of the new scheme are clearly seen.

(ii) *Including reassimilation.* Assimilation and forecasts were carried out over four periods. For each period a comparison was made with a forecast system that used envelope orography and the old gravity-wave-drag scheme. The data assimilation system is sensitive to the orography since the introduction of near-surface data and especially radiosonde data depends on the observing station heights. Consequently more data are used when the assimilating model uses mean orography. Three T106 L31 experiments for two-week periods in January, April and August, and a two-week T213 L31 experiment for March 1994 were run. The mean results for the three lower-resolution periods are similar to those

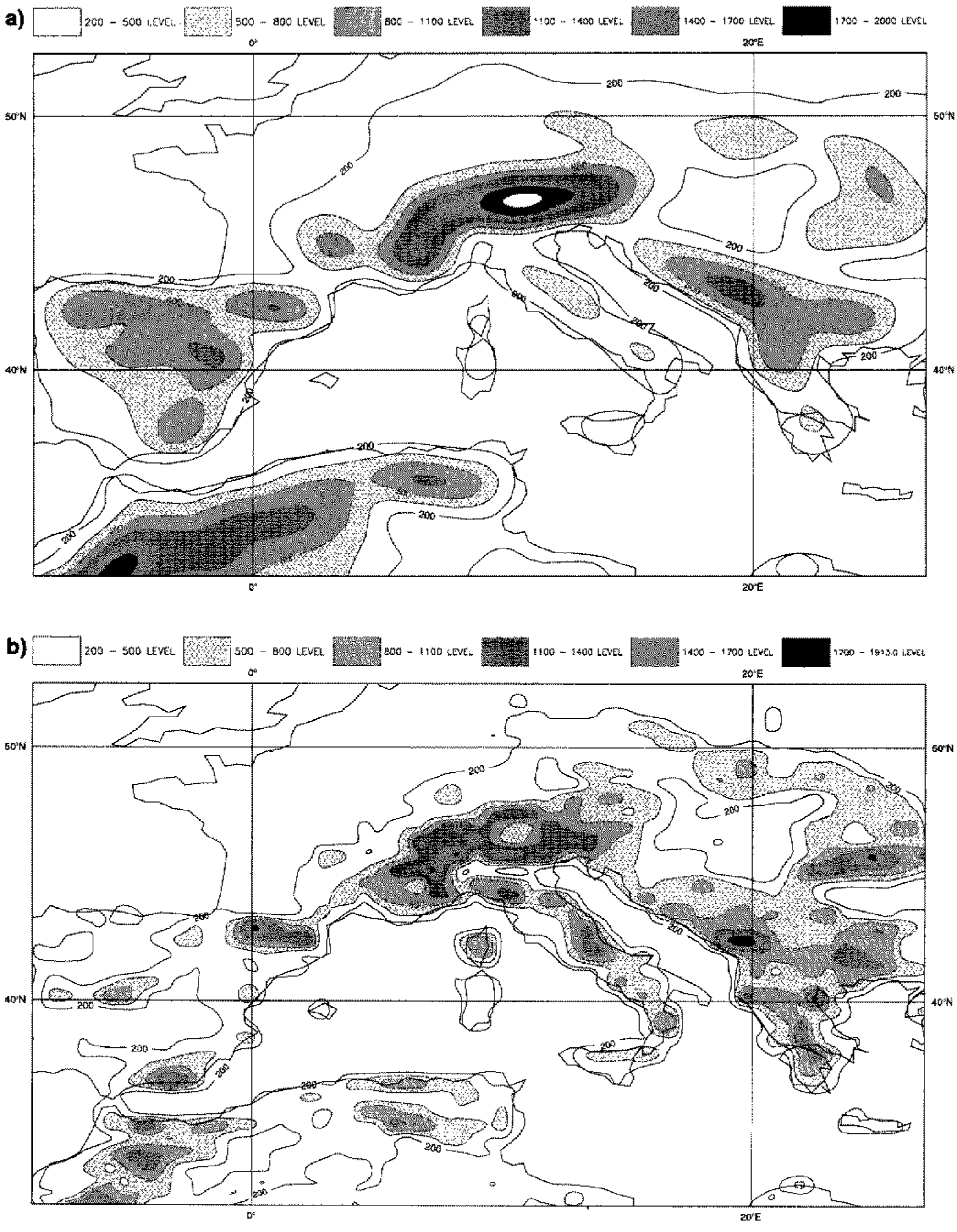

Figure 12. (a) The T213 orography; shading every 300 m. (b) The T213 'effective' orography increment computed from a 10-day forecast mean (initial date 15 January 1995).

in section 6(b), with a positive impact in January (Fig. 15(a)) and a near neutral one in August (not shown). The T213 (March) results are also slightly positive (Fig. 15(b)). There is a modest positive impact in the southern hemisphere, probably due to the use of mean orography in the data assimilation.

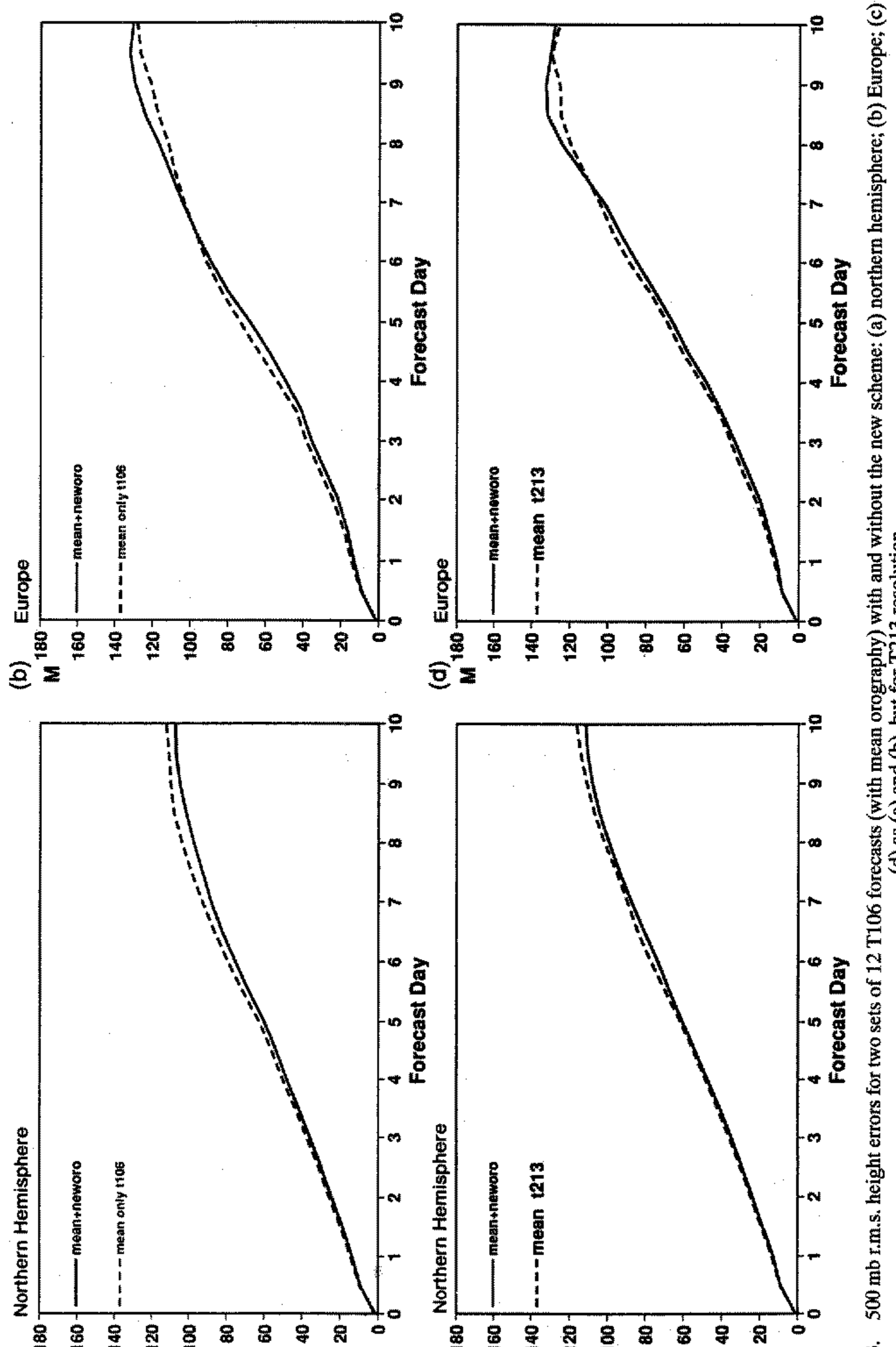

Figure 13. 500 mb r.m.s. height errors for two sets of 12 T106 forecasts (with mean orography) with and without the new scheme: (a) northern hemisphere; (b) Europe; (c) and (d) as (a) and (b), but for T213 resolution.

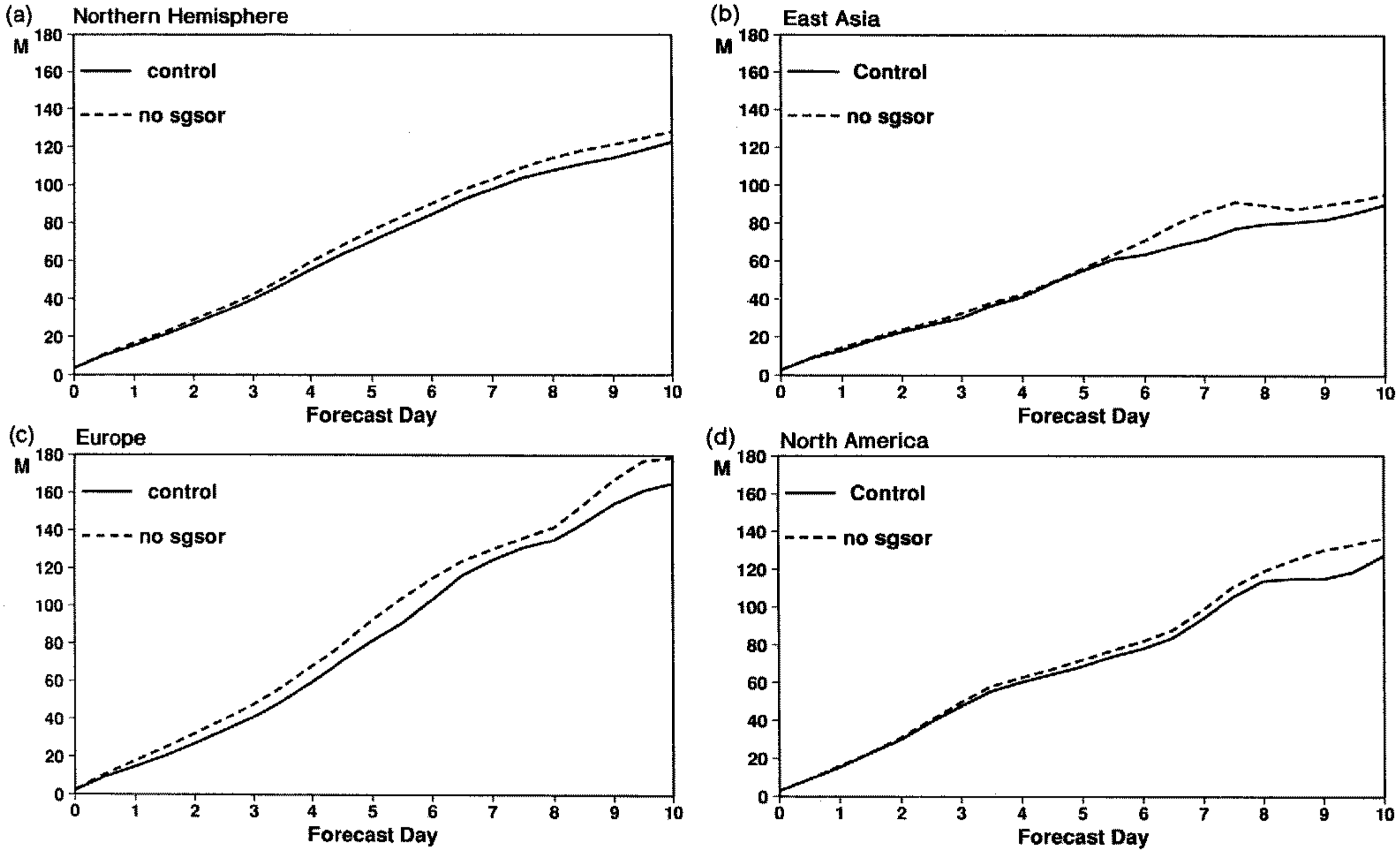

Figure 14. 500 mb r.m.s. height errors for two sets of 19 T213 forecasts (with mean orography) with and without the new scheme: (a) northern hemisphere; (b) Europe; (c) east Asia; (d) North America.

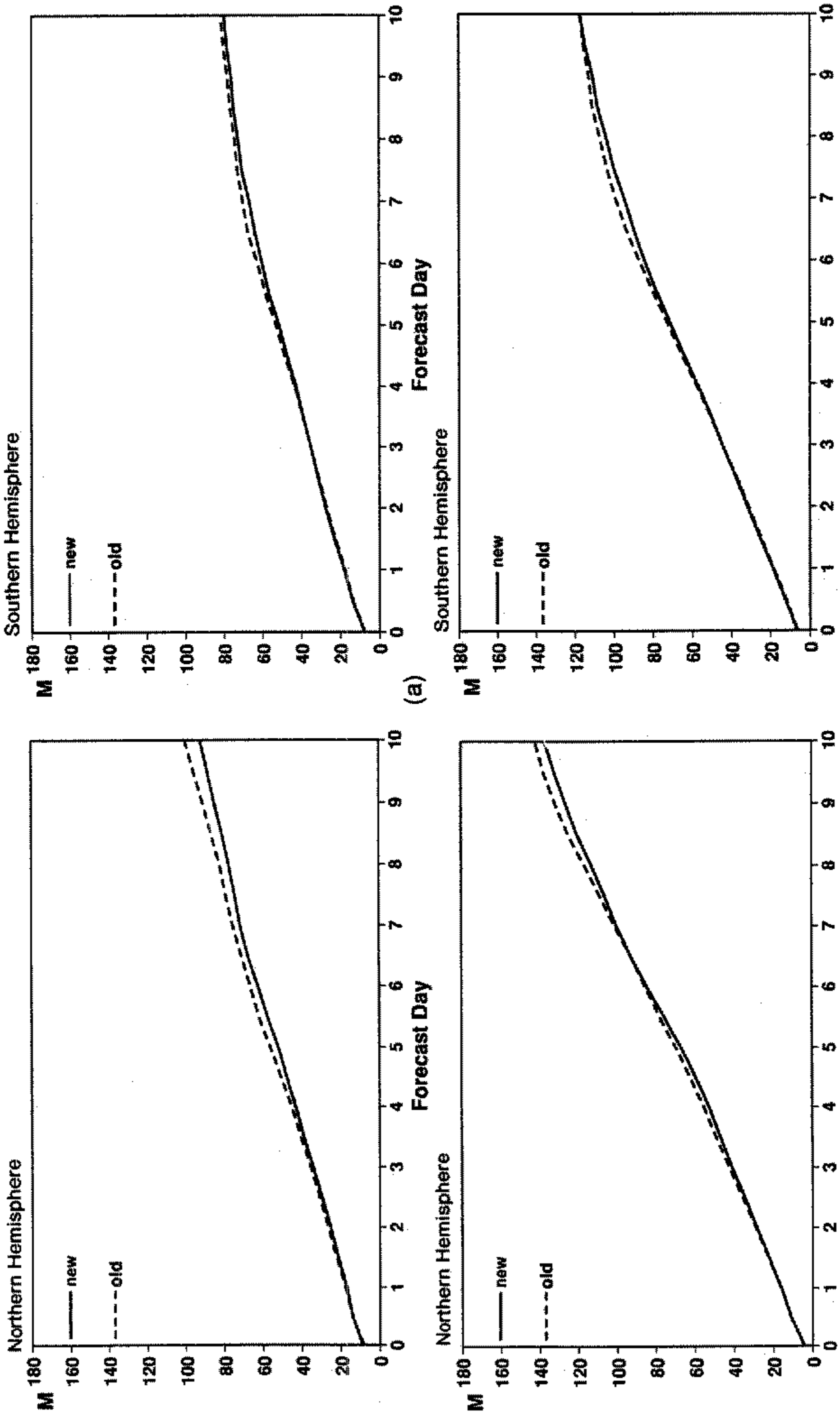

Figure 15. (a) 1000 mb (upper) and 500 mb (lower) r.m.s. height scores for fourteen consecutive forecasts (initial dates 2 January 1994–15 January 1994). Left-hand column: northern hemisphere; right-hand column: southern hemisphere. Forecasts and assimilation with T106 system; new scheme (with mean orography), continuous lines; old scheme (with envelope orography), dashed lines.

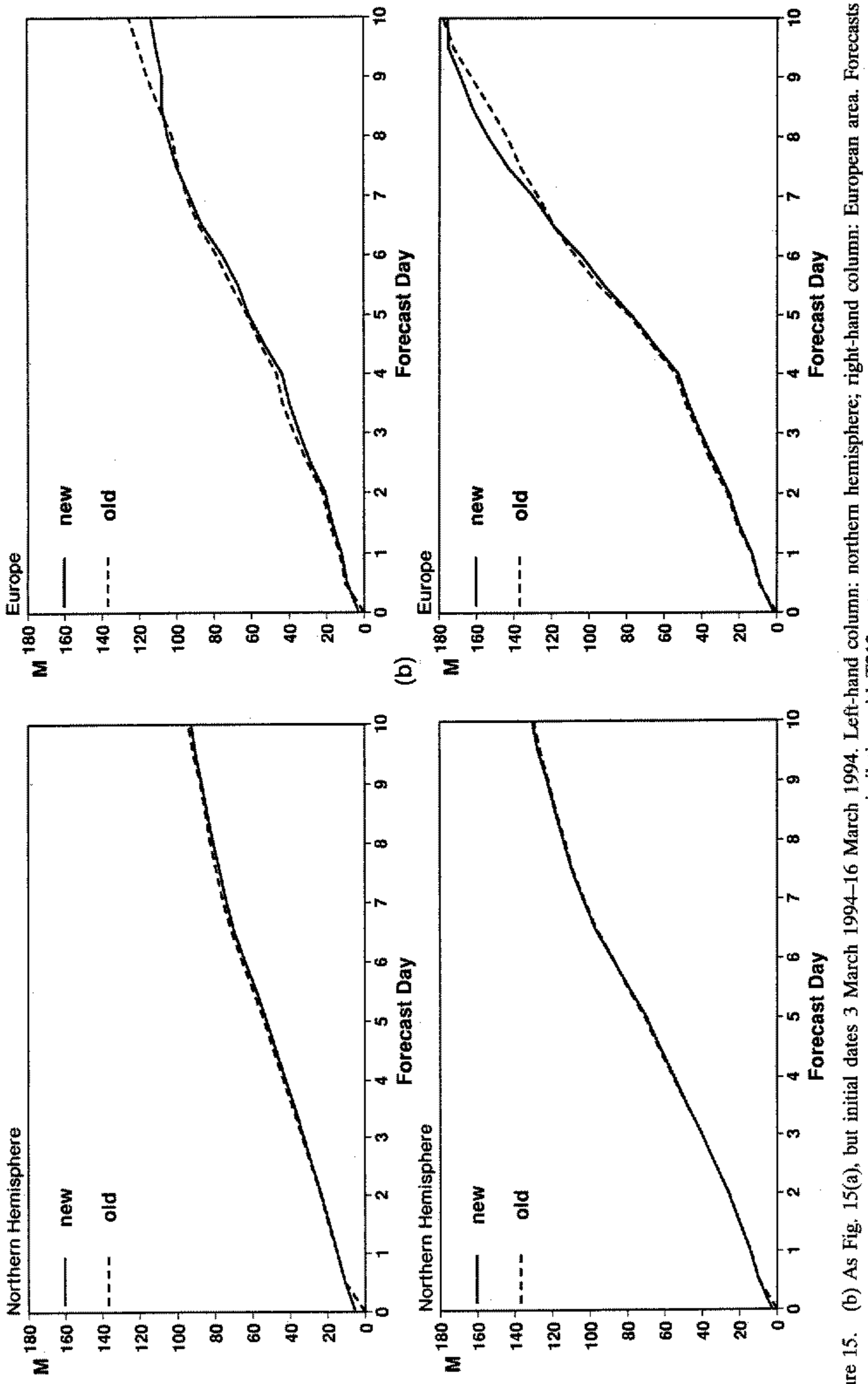

Figure 15. (b) As Fig. 15(a), but initial dates 3 March 1994–16 March 1994. Left-hand column: northern hemisphere; right-hand column: European area. Forecasts and assimilation with T213 system.

7. Concluding remarks

A new parametrization of subgrid-scale orographic drag has been presented. It encompasses recent developments in the nonlinear theory of stratified flows around obstacles. In this scheme, particular attention has been paid to the drag in the model layers of the atmosphere below the subgrid-scale mountain peaks. This low-level part of the scheme replaces the envelope enhancement of model orography. The upper part of the scheme still represents the role of gravity waves. This part has been revised to allow a better representation of mountain-ridge orientation and anisotropy. It also removes some arbitrary assumptions from the previous scheme. The depth over which the gravity-wave-drag part of the scheme is felt by the flow at low levels is now linked to dynamical properties of the mountain waves. The incident wind characteristics are calculated above the boundary layer (when the mountain is sufficiently high), suppressing the strong diurnal cycle which was found to occur in the old gravity-wave-drag scheme. The parameters of the new scheme have been calibrated using an off-line procedure, in which the scheme has been used to predict the mountain drag measured during PYREX. In this calibration, the new drag scheme outperforms the old gravity-wave-drag scheme, and fits well with the surface drag measured during field experiments. It also gives momentum flux vertical profiles that are more realistic than those of the old scheme. It was further shown that the new scheme has a realistic dynamical impact on the model dynamics in the vicinity of mountains, reinforcing the scheme's basic premise that mesoscale mountain drag slows down the low-level flow under most atmospheric situations. Results from forecast experimentation such as skill scores, precipitation amounts and distribution indicate that, overall, the combination of mean orography together with the new scheme performed better than the scheme using envelope orography plus the old gravity-wave-drag scheme. The new scheme is beneficial to the forecast skill of the ECMWF model at all forecast ranges and has been in operational use since 4 April 1995. The theoretical background to this work suggest that not only models of climate and GCM resolution but also much higher-resolution limited-area models should parametrize the drag due to the 'blocked' flow. As was noted in section 4, there remain considerable uncertainties in the direction of the mountain torque. Although the new scheme improves low-level flow deflection, by forcing the flow to be aligned with the ridge, thus minimizing the drag, flow deflection by subgrid-scale orography requires further study.

Acknowledgements

We thank P. Baines and T. Palmer for ideas and discussions which helped stimulate this research. Thanks also to P. Bougeault for providing the PYREX data at an early date and for additional derived data. A. Hollingsworth, J. C. R. Hunt, A. Simmons, T. Palmer and two anonymous referees provided constructive comments on the paper's first draft. The PYREX experiment was supported by Météo-France, INM (Spain) and CNRS (France).

Appendix

Specification of subgrid-scale orography

For completeness, the following describes how the subgrid-scale orography fields were computed by Baines and Palmer (1990). The mean topographic height above mean sea level over the gridpoint region (GPR) is denoted by $\bar{h}$, and the coordinate z denotes elevation above this level. Then the topography relative to this height $h(x, y) - \bar{h}$ is represented by four parameters, as follows:

(i) The net variance, or standard deviation, μ, of $h(x, y)$ in the GPR. This is calculated from the US Navy data-set or equivalent, as described by Wallace *et al.* (1983). The quantity μ gives a measure of the amplitude and 2μ approximates the physical envelope of the peaks (loc. sit.).

(ii) A parameter γ which characterizes the anisotropy of the topography within the GPR.

(iii) An angle ψ, which denotes the angle between the direction of the low-level wind and that of the principal axis of the topography.

(iv) A parameter σ which represents the mean slope within the GPR.

The parameters γ and ψ may be defined from the topographic gradient correlation tensor

$$H_{ij} = \overline{\frac{\partial h}{\partial x_i}\frac{\partial h}{\partial x_j}},$$

where $x_1 = x$, and $x_2 = y$, and where the terms may be calculated (from the USN data-set) by using all relevant pairs of adjacent gridpoints within the GPR. This symmetric tensor may be diagonalized to find the directions of the principal axes and the degree of anisotropy. If

$$K = \frac{1}{2}\left\{\overline{\left(\frac{\partial h}{\partial x}\right)^2} + \overline{\left(\frac{\partial h}{\partial y}\right)^2}\right\} \quad L = \frac{1}{2}\left\{\overline{\left(\frac{\partial h}{\partial x}\right)^2} - \overline{\left(\frac{\partial h}{\partial y}\right)^2}\right\} \quad M = \overline{\frac{\partial h}{\partial x}\frac{\partial h}{\partial y}}, \tag{A.1}$$

the principal axis of H_{ij} is oriented at an angle θ to the x-axis, where θ is given by

$$\theta = \frac{1}{2}\arctan(M/L). \tag{A.2}$$

This gives the direction where the topographic variations, as measured by the mean-square gradient, are largest. The corresponding direction for minimum variation is at right angles to this. Changing coordinates to x', y' which are oriented along the principal axes ($x' = x\cos\theta + y\sin\theta$, $y' = y\cos\theta - x\sin\theta$), the new values of K, L and M relative to these axes, denoted K', L' and M', are given by

$$K' = K, \quad L' = (L^2 + M^2)^{1/2}, \quad M' = 0,$$

where K, L and M are given by Eq. (A.1). The anisotropy of the orography or 'aspect ratio', γ is then defined by the equations

$$\gamma^2 = \overline{\left(\frac{\partial h}{\partial y'}\right)^2}\,\overline{\left(\frac{\partial h}{\partial x'}\right)^{-2}},$$

$$= \frac{K' - L'}{K' + L'} = \frac{K - (L^2 + M^2)^{1/2}}{K + (L^2 + M^2)^{1/2}}. \tag{A.3}$$

If the low-level wind vector is directed at an angle φ to the x-axis, then the angle ψ is given by

$$\psi = \theta - \varphi. \tag{A.4}$$

The slope parameter, σ, is defined as

$$\sigma^2 = \overline{\left(\frac{\partial h}{\partial x'}\right)^2}, \tag{A.5}$$

i.e. the mean-square gradient along the principal axis.

REFERENCES

Abarbanel, H. D. I., Holm, D. D., Marsden, J. E. and Ratiu, T. S. 1986 Nonlinear stability analysis of stratified fluid equilibria. *Phil. Trans. R. Soc., London, A*, **318,** 349–409

Baines, P. G. and Palmer, T. N. 1990 Rationale for a new physically based parametrization of sub-grid scale orographic effects. Tech. Memo. 169. European Centre for Medium-Range Weather Forecasts

Baines, P. G. 1995 *Topographic effects in stratified flows.* Cambridge University Press

Batchelor, G. K. 1967 *An introduction to fluid dynamics.* Cambridge University Press

Bessemoulin, P., Bougeault, P., Genoves, A., Jansa Clar, A. and Puech, D. 1993 Mountain pressure drag during PYREX. *Beitr. Phys. Atmos.*, **66,** 305–325

Boer, G. J., McFarlane, N. A., Laprise, R., Henderson, J. D. and Blanchet, J. P. 1984 The Canadian Climate Centre spectral atmospheric general circulation model. *Atmos.-Ocean*, **22,** 397–429

Bougeault, P., Jansa, A., Attie, J. L., Beau, I., Benech, B., Benoit, B., Bessemoulin, P., Caccia, J. L., Campins, J., Carrissimo, B., Champeaux, J. L., Crochet, M., Druilhet, A., Durand, P., Elkhalfi, A., Flamant, P., Genoves, A., Georgelin, M., Hoinka, K. P., Klaus, V., Koffi, E., Kotroni, V., Mazaudier, C., Pelon, J., Petitdidier, M., Pointin, Y., Puech, D., Richard, E., Satomura, T., Stein, J. and Tannhauser, D. 1993 The atmospheric momentum budget over a major mountain range: first results of the PYREX field program. *Ann. Geophys.*, **11,** 395–418

Bougeault, P. and Mercusot, C. 1992 'Atlas des réanalyses PERIDOT de l'expérience PYREX'. Note de travail No 8 du groupe de météorolgie à moyenne echelle. CNRM, F-31057 Toulouse, France

Clark, T. L. and Miller, M. J. 1991 Pressure drag and momentum fluxes due to the Alps. II: Representation in large-scale atmospheric models. *Q. J. R. Meteorol. Soc.*, **117,** 527–552

Egger, J. and Hoinka, K. P. 1992 Fronts and orography. *Meteorol. Atmos. Phys.*, **48,** 3–36

Etling, D. 1989 On atmospheric vortex street in the wake of large islands. *Meteorol. Atmos. Phys.*, **41,** 157–164

Gurevich, M. I. 1965 *Theory of jets in ideal fluids.* Academic Press

Haynes, P. H. and McIntyre, M. E. 1987 On the evolution of vorticity and potential vorticity in the presence of diabatic heating and frictional or other forces. *J. Atmos. Sci.*, **44,** 828–841

Hoinka, K. P. and Clark, T. L. 1991 Pressure drag and momentum fluxes due to the Alps. I: Comparison between numerical simulations and observations. *Q. J. R. Meteorol. Soc.*, **117,** 495–526

Howard, L. N. 1961 Note on a paper of John W. Miles. *J. Fluid Mech.*, **10,** 509–512

Hunt, J. C. R. and Snyder, W. H. 1980 Experiments on stably stratified flow over a model three-dimensional hill. *J. Fluid Mech.*, **96,** 671–704

Kirchoff, G. 1876 *Vorlesungen über mathematische physik.* Leipzig

Landweber, L. 1961 Motion of immersed and floating bodies. *Handbook of Fluid Dynamics.* 1st ed. McGraw-Hill

Lott, F. 1995 Comparison between the orographic response of the ECMWF model and the PYREX 1990 data. *Q. J. R. Meteorol. Soc.*, **121,** 1323–1348

Miles, J. W. 1961 On the stability of heterogeneous shear flows. *J. Fluid Mech.*, **10,** 496–508

Miles, J. W. and Huppert, H. E. 1969 Lee waves in a stratified flow. Part 4: Perturbation approximations. *J. Fluid Mech.*, **35,** 497–525

Miller, M. J., Palmer, T. N. and Swinbank, R. 1989 Parametrization and influence of subgrid-scale orography in general circulation and numerical weather prediction models. *Meteorol. Atmos. Phys.*, **40,** 84–109

Miranda, P. M. A. and James, I. N. 1992 Nonlinear three-dimensional effects on gravity waves: Splitting flow and breaking waves. *Q. J. R. Meteorol. Soc.*, **118,** 1057–1081

Palmer, T. N., Shutts, G. J. and Swinbank, R. 1986 Alleviation of systematic westerly bias in general circulation and numerical weather prediction models through an orographic gravity wave drag parametrization. *Q. J. R. Meteorol. Soc.*, **112,** 2056–2066

Phillips, S. P. 1984 Analytical surface pressure and drag for linear hydrostatic flow over three-dimensional elliptical mountains. *J. Atmos. Sci.*, **41,** 1073–1084

Schär, C. 1993 A generalization of Bernoulli's theorem. *J. Atmos. Sci.*, **50,** 1437–1443

Schär, C. and Smith, R. B. 1993 Shallow water flow past isolated topography. Part 1: vorticity production and wake formation. *J. Atmos. Sci.*, **50,** 1437–1443

Smith, R. B. 1979 Some aspects of the quasi-geostrophic flow over mountain. *J. Atmos. Sci.*, **36,** 2385–2393

1989 Mountain induced stagnation points in hydrostatic flows. *Tellus*, **41a,** 270–274

Smolarkiewicz, P. K. and Rotunno, R. 1989 Low Froude number flow past three-dimensional obstacles. Part I: baroclinically generated lee vortices. *J. Atmos. Sci.*, **46,** 1154–1164

Stein, J. 1992 Investigation of the regime diagram of hydrostatic flow over a mountain with a primitive equation model. Part 1: two-dimensional flows. *Mon. Weather Rev.*, **120,** 2962–2976

Tibaldi, S. 1986 Envelope orography and maintenance of quasi-stationary waves in the ECMWF model. *Adv. Geophys.*, **29,** 339–374

Wallace, J. M., Tibaldi, S. and Simmons, A. 1983 Reduction of systematic forecast errors in the ECMWF model through the introduction of an envelope orography. *Q. J. R. Meteorol. Soc.*, **109,** 683–717

Woods, J. D. 1969 On Richardson's number as a criterion for laminar–turbulent–laminar transition in the ocean and atmosphere. *Radio Sci.*, **4,** 1289–1298